Development of a Cadmium Zinc Telluride Based Gamma Camera for Simultaneous SPECT/MR Imaging

Development of a Cadmium Zinc Telluride Based Gamma Camera for Simultaneous SPECT/MR Imaging

By Erik Reimers, B.Eng

A Thesis Submitted to the School of Graduate Studies in the Partial Fulfillment of the Requirements for the Degree of Masters of Applied Science

McMaster University

M.A.Sc. (2021)

Hamilton, Ontario (Biomedical Engineering)

TITLE: Development of a Cadmium Zinc Telluride Based Gamma Camera for Simultaneous SPECT/MR Imaging

AUTHOR: Erik Reimers B.Eng (McMaster University)

SUPERVISOR: Dr. T. Farncombe

NUMBER OF PAGES: x, 87

Abstract

The current forefront of research in medical imaging technology includes working towards the combination of multiple imaging modalities into a single scan. SPECT is an imaging modality that would benefit from a combined approach with MRI allowing for improved diagnostic capabilities particularly in soft tissue regions. However, the traditional detectors used in SPECT are not capable of operating in the presence of an MRI magnetic field. This has led to the requirement for development of new gamma camera designs using modern solid state detectors.

We have developed the hardware and software for a gamma camera design using cadmium zinc telluride detector technology. The camera will be used in a SPECT system being made up of multiple individual gamma camera modules. These modules will be placed in a ring that can be inserted into the MRI bore as a stationary insert for simultaneous SPECT/MR imaging. Testing of the mutual compatibility of the two systems has led to the development of a gradient triggering hardware and software protocol. Subsequent testing of this method in a clinical 3T MR was performed. When gradient triggering was enabled, erroneous event data from the mutual interference was reduced to near zero levels and resultant images show no structural differences when compared to control acquisitions. During gradient application, the CZT modules are suspended, thus yielding a 60% drop in sensitivity due to the additional deadtime of the triggering. The produced MR image showed a reduction in SNR of 92%. Co-registration of the MR and gamma camera images was successfully performed, showing both the physical structural and radioactive activity distribution of the phantom.

Additionally, the potential of a diverging fan beam collimator for use in the multimodal SPECT/MR system was investigated using Monte Carlo simulations. Eleven collimator designs were compared, yielding between 13 to 23 modules per ring. The results showed that a practical SPECT/MR design using 18 detectors per ring with a 3.83

cm length collimator gave similar tomographic resolution to that of a clinical SPECT/CT system but with 7.0 times greater detection sensitivity compared to a conventional rotating dual-head camera. The simulations also showed that the system suffers from aliasing effects when reconstructing features of 7.9 mm or less. To further investigate how the design choices affected the tomographic resolution, parameters for collimator hole size, detector pixel size, and number of projection angles were also explored.

Acknowledgements

First and foremost my deepest appreciation to my supervisor, Troy Farncombe for his supervision and guidance throughout the completion of this project. You have truly been an amazing supervisor! I would like to thank Soo Hyun Byun and Mike Noseworthy for taking the time to be a part of my committee and their depth of knowledge for advice and teaching. I would like to acknowledge Norm Konyer for all the countless times that he has helped me with tests running the MRI scanner. This project would not have gone anywhere without your constant eagerness to help out. Finally thank you to my friends, family, and the Hollywood Homies for the unconditional love and support.

Contents

List of Figures

List of Tables

Chapter 1

Preface

The structure of this thesis begins in Chapter 2 with an introductory section on the motivation behind the project. It focuses on the use of multiple imaging systems, referred to as multimodality imaging and why it is important to today's healthcare system. This is followed by an introduction on the background theory for the project. This includes a brief explanation on the basic working mechanisms of SPECT and MRI, the difficulties faced when integrating the two modalities, the different detector options available for SPECT imaging, and a comparison of the research done thus far in the literature using these detection methods for multimodal SPECT/MR imaging. Next the concept of SPECT collimator design will be discussed, and finally the process that is involved for a Maximum Likelihood, Expectation Maximization (ML-EM) algorithm when used for SPECT reconstruction.

Chapter 3 then goes into the design choices and the process of development for the creation of a multimodal gamma camera for SPECT/MR. This includes discussion of the detectors, microcontroller, PCB, communication, and the software used to control the camera's operation.

Chapter 4 is an extended version of a paper submitted to the 2020 IEEE Nuclear Science Symposium Medical Imaging Conference Record. This paper looks at the results

for initial testing of the gamma camera design during simultaneous acquisition inside the MRI bore. In particular the work focuses on the effect of the MRI's magnetic field gradients on the detectors. The paper then goes on to investigate the testing performed for our solution to the mutual interference effects: a gradient triggering circuit and acquisition protocol.

Chapter 5 is another paper submitted to the 2020 IEEE Conference Record and looks at the simulations side of the project. Monte Carlo simulations were performed for potential SPECT/MR collimator designs. These collimators will be used for the SPECT ring which will be made up from the previously discussed gamma cameras. The paper looks at the option of a diverging fanbeam collimator geometry which would be pixel matched to the detectors. Comparison for length of collimators, number of cameras within the ring, collimator hole size, and the option of using alternative detectors with a smaller pixel pitch was carried out.

Although discussions are also presented in each paper, a further discussion and conclusion is given in Chapter 6. This short discussion looks at some of the potential shortfalls of the current design found in the results and compares them to other possibilities. Finally, Chapter 7 discusses potential future developments that can be applied to the project.

Chapter 2

Introduction and Background

2.1 Motivation

One in four people suffer from a form of brain illness at some point in their lifetime, making it one of the leading causes of ill-health worldwide (*WHO - World Health Report* 2001). These illnesses can advance quickly, leaving little to no time to provide effective treatment once symptoms present themselves (*WHO - public health challenges* 2006). To take on this world issue, we must bring together research and clinical knowledge from many fields of science and engineering. With neuroimaging techniques, we have the powerful ability to look into the brain and see how it functions. Therefore, pushing the forefront of the imaging technology used is key to improvements in brain research, among other areas of the body.

A major area of focus at the cutting edge of medical imaging technology today is the combination of multiple imaging techniques, known as modalities, into a single scan. The array of currently available modalities can be generalized into two categories: structural and functional. Structural imaging methods such as magnetic resonance imaging (MRI or MR) and computed tomography (CT) produce anatomical information of the body. These high spatial resolution approaches give detailed insights into changes that

have occurred on a structural level. Functional imaging methods, such as positron emission tomography (PET) and single photon emission computed tomography (SPECT), use radioactive compounds called radiotracers to visualize and characterize biological functions that are happening within the body. Although functional images are generally low-resolution, they allow for better understanding of how diseases function, going beyond what can be seen from a purely structural view. Detecting how diseases are progressing, the biodistribution of drugs throughout the body, and molecular events can all be visualized in real time. (Lee 2014; Cherry 2004)

The concept of multimodal imaging takes the complementary attributes of two methods and creates a single system which produces improved diagnostic abilities over individual conventional imaging. By combining structural and functional modalities, highly sensitive biological information can be precisely coregistered to a highly detailed structural image giving maximum diagnostic accuracy (Lee 2014). Hybrid systems which combine CT with PET or SPECT have become the clinical standard for many diseases involving brain, heart, and bone (Patton 2009). The future of multimodality imaging is now looking at the replacement of CT with MRI, creating innovative hybrid PET/MR and SPECT/MR systems. Compared to PET/CT and SPECT/CT, these cutting edge machines will take advantage of MRI's higher soft tissue contrast and absence of ionizing radiation for the structural component of the image. Although these are important advantages for the entire body, they are particularly appealing to neuroimaging due to the brain's soft tissue makeup and sensitivity (Lee 2014). Additionally, there is the opportunity for more advanced imaging techniques which could make use of the wide array of applications for MRI beyond just serving as a structural anatomical reference.

Currently, at the time of writing, hybrid PET/MR machines have been commercially produced and can be found in several major hospitals across Canada (*GE SIGNA™ PET/MR* n.d.; *Canadian Healthcare* 2018). Although the modality is still in its clinical

infancy, studies have shown success in a wide variety of applications (Ehman 2017). On the other hand, the development of SPECT/MR has lagged behind. However, for certain applications, SPECT does offer advantages over PET causing there to still be the desire for a simultaneous SPECT system (Carminati 2018). Primarily, there is the wider availability and lower cost of operation. SPECT does not require an in hospital, on site production of its radiotracers (using a cyclotron machine), which is the case for some PET radiotracers. Because the radiotracers used in SPECT generally have longer half-lives before decaying, they can be ordered and produced off site, allowing for greater flexibility and lower cost (Carminati 2018). Due to the lower cost, SPECT is often more commonly used in hospitals than PET (Bailey 2013). An additional advantage is the potential for simultaneous multi-tracer acquisition. Because of the radioactive decay mechanism used in PET imaging, all PET tracers emit identical energy, indistinguishable photons when the decay occurs. This is not the case in SPECT, which allows for multiple tracers to be used simultaneously and their unique photon energies to be separated into individual images for each tracer type used. This gives the opportunity for examination of multiple direct biologic pathways all during a single scan (Bailey 2013). In particular, such a SPECT/MR system may have application in some cardiac, brain, breast, or theranostic applications (Yang 2018; Lai 2018). Here we present the development of a detector module system with the ultimate goal of developing a full-ring SPECT insert for simultaneous SPECT/MR imaging.

2.2 Nuclear Medicine

Nuclear medicine is a branch of medical imaging which uses radioactive isotopes to look at functional processes occurring inside the body. These specialized radioactive isotopes, called radionuclides, are attached to a compound that targets the functioning of a specific biological pathway. Once labeled with the unstable isotope, the compound is called a radiotracer, and is administered to the patient. These tracers act like natural

products in the body, traveling throughout and following the functional path of interest. The radioactive isotopes eventually undergo radioactive decay, causing the emission of gamma rays from inside the body. Collection of these photons by detectors placed around the patient allow for localization of where the photons originated, and in turn, where the tracers traveled during their time in the body. This knowledge then gives important insight on how the biological pathway of interest is functioning. (National Research Council (US) 1996)

Within the field of nuclear medicine, two main techniques exist: single photon emission computed tomography (SPECT) and positron emission tomography (PET). These two imaging methods, called modalities, differ fundamentally based on the type of radionuclide use. In SPECT, all radionuclides emit a single photon gamma ray when decaying. Through the use of collimating holes and multiple planar images taken at angles around the body, localization of where the decaying events took place can be determined. A set of slices, called tomographs, which form a 3D image, are produced using the planar images and show the tracer distribution within the body. In PET, the radionuclides used are instead positron emitters. After decaying, these released positrons quickly undergo annihilation with a nearby electron emitting two identical gamma rays at 180 degrees from one another. With a ring of detectors around the patient, these two gamma rays can be collected as a pair and again, localization and a 3D image of the tracer distribution is produced. (National Research Council (US) 1996)

2.3 Magnetic Resonance Imaging

Magnetic resonance imaging is another imaging modality commonly used in hospitals which shows detailed anatomy of the organs and can also show physical processes within the body. The imaging technique is primarily based on detecting the hydrogen nuclei (single protons) within the body. Protons have a quantum spin property, described by

the gyromagnetic ratio ($\gamma_H = 42.58$ MHz/T). This spin property results in a magnetic moment vector for the atom. When the hydrogen atoms within our body are placed in a static magnetic field of strength, B_0 such as in an MRI bore, a small proportion of the protons' vectors will line up parallel or anti-parallel to the direction of the magnetic field flux lines. This organization of the magnetic moment vectors creates a net longitudinal magnetization. These protons can be visualized as precessing around this direction according to the Larmor frequency, ω, described in the gyromagnetic ratio equation, $\omega = \gamma_H B_0$. For a 3.0 T MRI machine imaging hydrogen, the frequency of interest is then approximately 128MHz.

Next, during the process of an MRI sequence, the protons are excited using a radio frequency (RF) pulse from the MRI transmit coils. By using an RF frequency equal to the Larmor frequency of the protons, they absorb the energy of the pulse, inducing a transverse magnetization into the system. This process is visualized as flipping the protons' net magnetization vector into the transverse plane, by a specified flip angle. In their flipped state, the protons are unstable and will relax to their initial state. This relaxation process gives off their own RF signal, which is called the free induction decay, and is detected by the MRI receive coils. The timing of their free induction decay is described by two parameters commonly referred to in MRI sequences: T1 and T2. T1 describes the time taken for the longitudinal magnetization to relax back to it's initial maximum value parallel to B0, and T2 describes the time taken for the transverse magnetization to dephase and return to zero. Changes to the MRI sequence parameters allow for the image to be primarily T1 or T2 weighted. Depending on the chemical makeup of the object being imaged, these timing values will be different, allowing for contrast in the image. For example, fat will appear dark and water will appear bright according to their T2 values.

As described thus far, during the free induction decay process there is no way for

localization of where the RF free induction decay is originating from. This step is done using magnetic field gradients, of which there are three (one for each axis: x, y, and z). For localization, the gradients are used to add an additional magnetic field on top of the static field. These new fields vary linearly across the bore, creating differing Larmor frequencies at different locations within the physical space. First, the slice select gradient is turned on and added to the field. The MRI is then capable of exciting only a single slice of the physical space with its RF pulse. This is because only a select region of protons will be precessing at the matching Larmor frequency to the RF pulse frequency. Using the remaining two gradients, the frequency encoding and phase encoding gradients, further localization within that slice is performed. Using a series of steps which turn on and off the gradients, a full 3D acquisition of the body is created. The time taken between each excitation RF pulse is called the repetition time (TR) and can occur hundreds of times in a single scan. (Weishaupt 2006)

2.4 Implementation of Simultaneous SPECT/MR

The concept of multimodal imaging takes into account that different methods have complementary attributes and that no single imaging method can show all the information of another. By combining the complementary attributes of two methods and creating a single system, the new multimodality system can produce improved diagnostic abilities over individual conventional imaging (Zhang 2020). Simultaneous imaging from the two modalities is generally preferential. This is due to three reasons: (1) removal of patient movement between scans which can lead to inaccurate coregistration of the two images, (2) reduction in hospital time, and (3) the ability to run dynamic acquisitions in which both modalities are creating spatial and temporal data sets simultaneously, looking at a process occurring over time (Hamamura 2010; Geotz 2008).

In particular to the integration of SPECT and MRI, there are a number of factors that

must be considered when designing such a system. To start, the location of the gamma ray detectors and associated electronics used in the SPECT system must be considered. Detectors, collimators, computers, circuit boards, cables, and communication methods must all be taken into account. If they are placed within the MRI bore, they will be introduced to the strong static magnetic field, switching gradient fields, and the RF pulses, and must still be capable of operating. Additionally, there is limited space within the bore of the MRI, requiring the SPECT system to have a small physical footprint. Alternatively, if they are placed outside the bore, within the MRI components, extensive reengineering of the MRI system must be carried out.

Looking at the problem from the other side, the SPECT detectors and associated electronics must not negatively affect the MRI operation. First, the magnetic field homogeneity is crucial to the MR image's geometric accuracy (how accurately the MR image represents the true geometry of the anatomical structure being imaging). If the magnetic field becomes non uniform within the imaging region, the location where the signal is being detected from is no longer accurate and the MRI cannot reliably reproduce the structure. Magnetic susceptibility is the property of how well a material will become magnetized when placed in a magnetic field. Ferromagnetic materials have large magnetic susceptibilities and will therefore considerably alter the homogeneity of the field, causing poor geometric accuracy and perhaps even damage the MRI machine. However even non-ferromagnetic materials have some degree of magnetic susceptibility and must also be taken into account.

Secondly, because the signal acquired during an MRI sequence is very weak, the MRI is sensitive to any outside RF interference. In particular, frequencies near the operating frequency of 128MHz can be particularly detrimental to MRI performance. In fact, great care is taken when designing the MRI room to prevent any interference from other parts of the hospital. When considering the design of the SPECT detectors and associated

electronics, electromagnetic interference (EMI), which is the production of unwanted RF noise from the electronics, must be considered. EMI can be generated from all aspects of powered electronics due to the acceleration of charged particles within the system from electrical currents. Techniques such as a Faraday cage can be used to help shield the system and prevent unwanted outgoing and incoming RF noise, limiting this effect. (Hutton 2016)

2.5 Common Detector Options Used in SPECT

2.5.1 Scintillators and Photomultiplier Tubes

The detection method of a scintillator crystal coupled to a photomultiplier tube (PMT) has been the traditional method for clinical SPECT and PET imaging (Hutton 2018). A scintillator is a type of material (usually a sodium iodine crystal (NaI(Tl)) in the case of SPECT) that undergoes the process of scintillation when excited by ionizing radiation, such as a gamma ray. When the gamma ray hits the crystal, it interacts with the crystal lattice causing the photoelectric effect. This excites multiple electrons from the valence band to the conduction band leaving behind a hole. A decay will then occur causing the electrons to drop back into their lower energy state. This final stage releases further photons of lower energy and the process of scintillation. In the case NaI(Tl), these lower energy photons are in the visible spectrum and are then used to detect where the original gamma ray was incident on the crystal. (*Stanford* 2009)

However, this emitted light is too weak to be visualized directly, and so the light produced from the scintillator crystals must be amplified in some way, traditionally done using photomultiplier tubes (PMTs) (Fig. 2.1). The PMTs are used to convert light into an amplified electrical signal. This is done through a series of metal plates called dynodes which have large potential voltages biased across them. As the electrons are accelerated across the dynodes from a photocathode to an anode, impact ionization occurs releasing

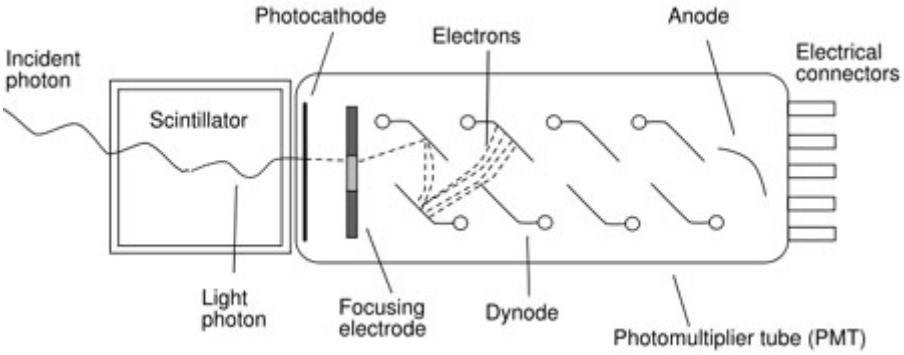

FIGURE 2.1: Diagram of a scintillation crystal in conjunction with a photomultiplier tube. (*Stanford* 2009).

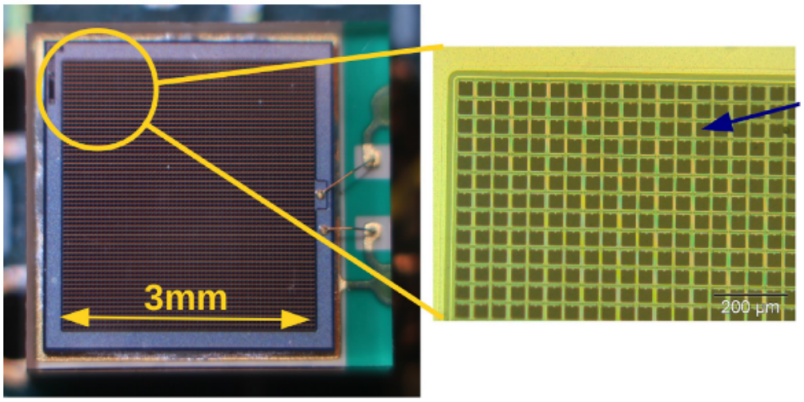

FIGURE 2.2: Photo of a silicon photomultiplier detector. A zoomed in view of the detector shows the dense array of individual single photon avalanche diodes. (Hamamatsu n.d.)

.

more electrons and amplifying the electric signal. This electric signal is then measured as a current using electrical connectors, and recorded for later reconstruction of the image. Because multiple PMTs will see visible light from a single gamma ray interaction, a basic logic pattern using the signal intensities is employed to localize where the event initially occurred. (Polyakov n.d.)

2.5.2 Silicon Photomultipliers

A silicon photomultiplier (SiPM) is a solid state semiconductor photodetector and is considered the successor to the PMT (Fig. 2.2) (Trigilio 2018). Still used in conjunction

with a scintillator crystal, the SiPM does not need a large footprint of dynodes to amplify the weak visible light. Instead, the silicon absorbs the photon, creating an electron-hole pair which accelerates within the substrate due to semiconductor doping regions and an electric field bias. With a sufficiently high electric field strength, it is possible to give the charge carrier enough kinetic energy to undergo impact ionization. This process perpetuates and amplifies the response, allowing for measurement of the event. A silicon photomultiplier is made up of a dense array of small, independent sensors called single photon avalanche diodes. As with PMTs, a logic pattern is again used to localize the event location and to simplify the electronics. (*SensL - Introduction to SiPM* 2011)

2.5.3 Cadmium Zinc Telluride Detectors

Cadmium zinc telluride (CZT) detectors are a third gamma ray detector option which could potentially be used in a SPECT/MR system (Fig. 2.3). These detectors allow for direct radiation detection and do not require a scintillator crystal to operate. They again use a solid state substrate (made of a CZT lattice) and use a strong electric field bias. However, when ionizing radiation such as a gamma ray interacts with the substrate, it directly undergoes the photoelectric effect, creating electron-hole pairs. The number of electron-hole pairs are proportional to the energy of the photon. These charge carriers are then measured as a current between the electrodes and the gamma ray event is recorded.

Alternatively to scintillation based methods, the CZT substrate is divided into individual pixel regions, allowing for direct localization of the gamma ray interaction. (*Advatech UK - Overview of CZT Radiation Detectors* n.d.)

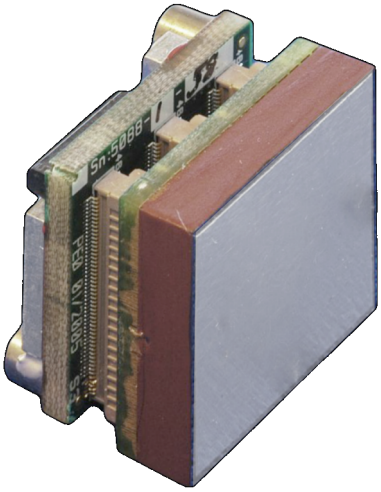

FIGURE 2.3: Photo of a cadmium zinc telluride detector. The CZT substrate is visible with the associated readout electronics positioned behind. (*Ideas SRE4001* n.d.)

.

2.6 Comparison of Detector Technologies for SPECT/MR

The possibility of a truly integrated, simultaneous SPECT/MR system has come about from the advancement of new detector technologies. While in a strong, clinically relevant, magnetic field (either 1.5 T or 3.0 T), moving electrons are subjected to considerable Lorentz forces. This force, $\vec{F}$, is described as $\vec{F} = q\vec{v} \times \vec{B}$, where q is charge, $\vec{v}$ is the velocity vector of the particle, and $\vec{B}$ is the strength vector of the magnetic field. This force causes an acceleration perpendicular to the velocity direction. The longer the distance the electron travels through the magnetic field the greater the effect.

Due to the long distances traveled by the electrons, the standard detectors used in SPECT (the previously discussed vacuum tube technology of scintillator crystals in conjunction with PMTs), are not capable of operating in the presence of an MRI magnetic field. This has now changed with the arrival of the modern solid state detectors: SiPM and CZT detectors. With SiPMs being an photodetector analogue readout of light from scintillators using logic pattern for localization, and CZT detectors being a direct

conversion, digital pixelated array.

When comparing the two, SiPMs have been the first choice for PET/MR integration. This is due to their superior timing performance compared to CZTs. Fast timing information is required for PET's short timing window (Wagenaar 2006; Wehner 2014). However, for SPECT/MR, the choice of SiPM or CZT has been divided, with fairly equal research having been done using each detector type. As an introduction to the concept of CZT use in SPECT/MR, in 2006 D. Wagenaar et al. showed the capability of CZT detectors to operate inside a static 3T MRI field with no significant interference (Wagenaar 2006). Following this, from 2010 to 2013, several groups then began developing CZT based SPECT/MR designs mainly for small animal testing (Hamamura 2010; Meier 2011; Cai 2013b; Cai 2013a). Their research found mixed success when looking at metrics of system resolution and mutual interference. In order to operate, some of the designs still used rotating camera acquisition protocols similar to traditional systems. This was done to acquire more projection angles for improved tomographic resolution or to create an averaged MR image as an attempt to remove mutual interference artifacts. Rotation of the camera has since been deemed undesirable for truly simultaneous SPECT/MR due to the limitations of motors and moving parts while the MRI is acquiring (Carminati 2018). However their research did point to a major advantage for CZT detectors over SiPM detectors (of which were already being used in more progressive PET/MR research). This is the improved energy resolution. In contrast to the inefficient process for the conversion of incident gamma rays to charge signals in scintillation detectors, a semiconductor CZT detector uses direct-conversion. This allows for a higher statistical pairing between the charge carriers and the incident photon energy, resulting in a reduction in the uncertainty when making a measurement of the photon energy. Further statistical fluctuations found in scintillation detectors from non-uniform light output along the crystal length and susceptibility to dark current results in relatively low energy resolutions overall from scintillation methods. (Wagenaar 2007; Iniewski

2014; Tao 2012)

The energy resolution of the system is used to select for only counts which match the desired energy of the radioisotope being imaged and to ignore other counts from scatter and background which can be considered noise. With improved energy resolution this allows for narrower windowing around the energy peak of interest without considerable loss in sensitivity, ultimately improving the final image's signal to noise ratio (SNR). The narrow energy windowing also then allows for better discrimination of isotopes when performing multi-isotope studies. Disadvantages of CZT presented by the groups include: (1) a small shift in the signal charge during the substrate detection mechanism due to the Lorentz force from the magnetic field, and (2) CZT requires direct readout of each pixel leading to more complex electronics and larger footprint size inside the bore.

More recently, the research in SPECT/MR has been largely produced by a multi-group collaboration with their INSERT project first presented in 2014 (Salvado 2014). These groups have selected a design architecture using SiPMs, taking advantage of the wide depth of research and development that these detectors have undergone for PET/MR development. They make the case for SiPMs, claiming superior MRI compatibility due to no intrinsic sensitivity to magnetic fields and a smaller size. Although energy resolution of SiPMs is still inferior, they claim it will still be adequate for common multi-radionuclide acquisitions with a goal of 12% FWHM energy resolution at 140 keV. This is in comparison to traditional PMT SPECT offering ∼10% resolution and CZT SPECT detectors which can offer ∼5% resolution. (Carminati 2019)

2.7 SPECT Collimator Design

The principle of SPECT imaging relies on the concept of ray tracing. Information of where on the camera the incident gamma photon was detected, and the angle that the ray arrived at is required. Then using this information for all the events collected, the

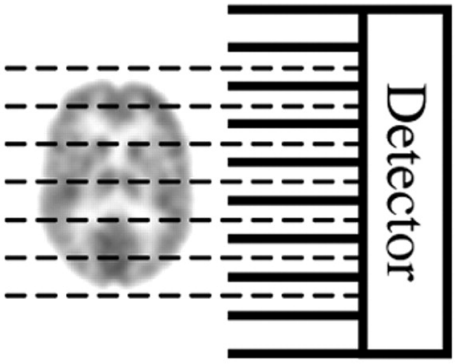

Figure 2.4: Diagram of a parallel hole collimator. (Accorsi 2008)

.

final image can be reconstructed to determine the original distribution of the radioactive tracer within the body. Using an array of detectors or individual pixels, the location of incidence can be determined. However to determine the angle of incidence, a collimator must be used. The collimator is placed in front of the camera and allows the reconstruction algorithm to map lines of response to particular detector positions.

In the case of a parallel hole collimator, the lines of response are created using a thick block with an array of parallel holes placed throughout (Fig. 2.4). By using a material such as lead with a high stopping power for gamma rays, only rays which arrive at the collimator traveling parallel to the holes will continue on and reach the detectors. Any incident rays at angles other than parallel will be attenuated by the lead material that separates the holes, called the septal. Because of this, only a small fraction of the emitted photons actually pass through the collimator holes and are detected. This property is called sensitivity, and is defined as the ratio of total emitted photons to total detected photons. By increasing the hole size, sensitivity will improve, however the lines of response used for reconstruction are now less precise. This then leads to a reduction in image resolution. This resolution-sensitivity trade off is commonly considered, and the ideal balance is often application specific.

The collimator is also responsible for controlling the field of view (FOV) of the gamma camera and in turn the SPECT system. By using holes that are not parallel (called a fanbeam collimator), the lines of response now encompass a different physical space, changing what volume in front of the camera it is capable of imaging. Several collimator designs have been developed for common clinical use and offer different advantages for specific applications.

For example in small animal imaging or small organ imaging such as thyroid imaging, a high resolution is often the primary goal, with low sensitivity and a small FOV being an accepted trade off. With this in mind, a pinhole collimator is often the chosen design for this application. A pinhole collimator consists of a single cone hole (although more complex multi-pinhole design are also used) which projects the FOV onto the imaging plane. The pinhole design offers high resolution and high magnification, but suffers from poor sensitivity due to the limited number of holes allowing photons through.

In contrast, for gated cardiac imaging the images must be acquired quickly with the rhythm of the heart rate. In this case, sensitivity is of most importance and is generally considered to be more important than the resolution of the image. In this scenario, a parallel hole collimator may be chosen. Additionally, resolution can be improved by reducing the FOV to only include the organ of interest by using a fanbeam collimator. More complex designs such as multi-pinhole and slit-slat collimators are continually being investigated to try and improve on the current technology. (Audenhaege 2015)

2.8 SPECT ML-EM Algorithm Reconstruction

When acquiring a SPECT image, the radionuclides in the tracers decay and release gamma rays from within the body. If these gamma rays pass through the collimator and are detected, a set of projection images can be produced over varying angles around the patient. The next step is to use these projections to reconstruct a 3D distribution map of

the tracer distribution within the body. The process of the photon leaving the body and being detected is referred to as the forward projection. The goal of reconstruction is to apply a back projection to the set of projection images or to "solve" the inverse problem. The most commonly used method for reconstruction is an iterative statistical approach. Although many more complexities can be added, the basic form of a SPECT maximum-likelihood expectation-maximization (ML-EM) algorithm is summarized below.

First, the physical 3D space that is to be reconstructed is discretized and reshaped into a column list of B voxels, where the value of each voxel, $\lambda(1)...\lambda(b)...\lambda(B)$, represents the maximum likelihood tracer distribution within its volume. The projection images, which are already discretized as pixels in a set of images, are also reshaped into a column list of, D, pixels and their values, $n^*(1)...n^*(d)...n^*(D)$, are the number of events counted during acquisition from their pixel area. Because of the collimator, each detector pixel only sees a limited line of sight into the voxel space. A ray mapping matrix, referred to as the probability matrix, G, can be created which maps the probability that a given voxel is seen by a given pixel, and vice versa. This is done either analytically with a geometric model of the collimator, or empirically using a Monte Carlo simulation.

To create the probability matrix, G, a collimator model must be determined which describes the planar point spread function (PSF) of the camera-collimator system. The PSF model is often expressed as the full-width at half-maximum (FWHM) of the response as a function of distance from the imaging plane. Analytically this can be done by ray tracing the photon path from the point source back to the imaging plane and calculating the attenuation by the septal material. For example, a parallel hole collimator FWHM resolution, R, can be described analytically as $R(h) = d(a + h)/a_{eff}$. Where h is the distance from the object to the imaging plane, a is the length of the collimator, a_{eff} is the effective length of the collimator taking into account penetration effects, and d is the hole diameter as described in Fig. 2.5. (Audenhaege 2015)

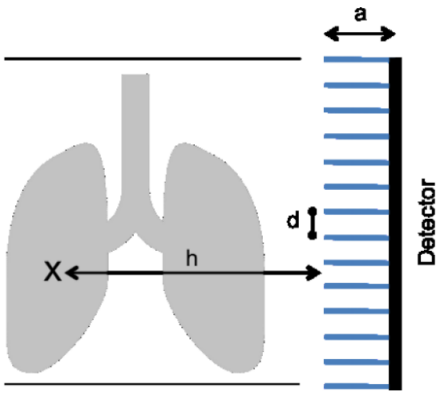

FIGURE 2.5: Diagram of a parallel hole collimator used for the analytical calculation of the system's PSF. (Audenhaege 2015)

Empirically, the PSF model can be determined by running multiple Monte Carlo simulations with a point source positioned at varying distances in front of the camera-collimator system. The FWHM of the resulting PSF images can then be fit to a trend creating an empirical collimator model.

Next the probability matrix, G, can be created. This is done by mapping the line of response of each voxel back to the imaging plane. The distance from the voxel to the imaging plane is used along with the PSF model to create a PSF response on the imaging plane centered at the voxel's line of response location. This PSF response matrix for the voxel is reshaped into a column list and stored as the first column of the G matrix. The entire G matrix is populated by creating PSF responses for each voxel. The probability matrix, G, can then be used to describe the probability that a given pixel is seen by a given voxel, and the transpose of the G matrix can be used to describe the probability that a given voxel is seen by a given pixel.

The iterative process using k iterations then follows the simplified flow chart shown below (Fig. 2.6). For the first iteration ($k = 1$), an initial estimate of 1 for the tracer distribution is made for each voxel, $\lambda^{k=1}(1 : B) = 1$. A forward projection of this estimate onto all the pixels, n_i, is then calculated using the probability matrix, $n_i =$

$\sum_{j=1}^{B} G_{ij}\lambda_j$. This forward projected estimate is compared to the true projections taken during the acquisition. The element-wise division of the two sets of projections results in a correction term, $n'_i = n^*_i./n_i$, which represents how well our current guess of the tracer distribution matches the set of true projection images. This correction term is then back projected into a set of correction voxels, $x_j = \sum_{i=1}^{D} G_{ji}n'_i$. The correction voxels are normalized, $x'_j = x_j./\sum_{i=1}^{D} G_{ji}$, and used to update our current estimate based on the corrections seen, $\lambda_j^{k+1} = \lambda_j^k \cdot * x'_j$. This updated estimate, λ^{k+1}, is then used as as the current estimate for the next iteration. Eventually the normalized correction term voxels will approach unity which shows that the current estimate of tracer distribution matches the actual projection images taken during the SPECT acquisition. (Shepp 1982)

A further complexity can be added to the process called ordered subset expectation maximization (OSEM). Using this method, the set of projection images are divided into subsets (2 or more subsets). During the back projection phase of the algorithm, each subset of projection data is back projected individually and used to update the current estimate. By using OSEM, the current estimate is updated more frequently (more than once per iteration). This has been found to accelerate the image reconstruction speed of the algorithm with a speed-up factor approximately equal to the number of subsets in which the projection data are divided. (Branderhorst 2010)

Figure 2.6: Flowchart of the iterative ML-EM algorithm.

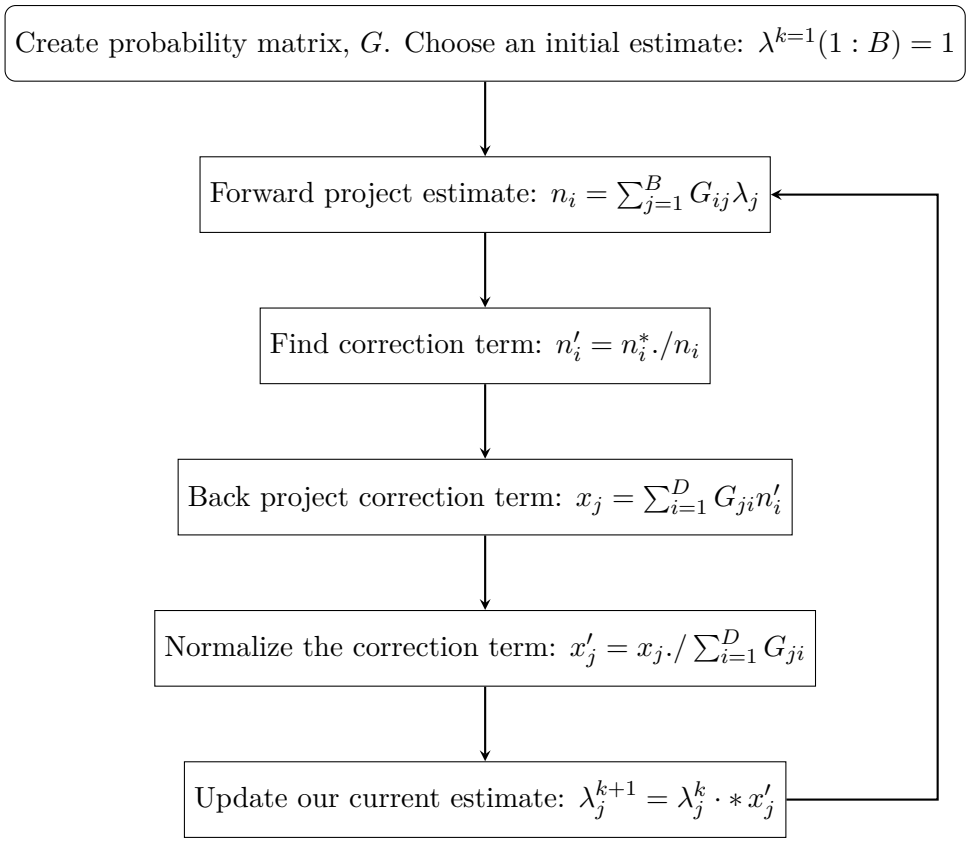

Chapter 3

Hardware and Software Development

3.1 Project Design

The foundation of the project was initially laid out by previous work done by Ashley Tao (Tao 2016b) with her development of an MR-compatible gamma camera for combined molecular/MR breast imaging. For this project, the application was changed to a generalized, full-ring SPECT system for SPECT/MR. Although many of the design considerations could be adopted over, several key architecture decisions were reevaluated.

The newly envisioned full-ring SPECT system will be made up of multiple individual gamma camera modules. These camera modules can be developed and tested individually allowing for rapid iteration and prototyping. The camera modules will then be placed in a stationary ring providing multiple projection angles of the patient. This ring will be capable of being inserted into the bore of an existing MRI machine without any alterations, and allow for simultaneous SPECT/MR imaging of the two modalities. For initial testing of the hardware viability, a single gamma camera module was developed. With sufficient results, the camera module can then be scaled into a full SPECT system.

The footprints of the camera modules were also given the design goal to be as compact as possible using a single printed circuit board (PCB) with all electronic components placed horizontally to one another. These flat modules are then positioned around the edges of the MRI bore away from the patient. This architecture allows for more space within the ring expanding the possible applications of the system and reducing chances of claustrophobia.

3.2 Detectors

The basis of the design uses solid state cadmium zinc telluride (CZT) detectors. The alternative detector technology discussed previously, which is used in most current PET/MR designs, are SiPM detectors (Muzic Jr. 2014). However, from previous investigation, the use of SiPMs were found to be prone to excess dark current and resulted in inadequate energy resolution when coupled to relatively slow CsI(Tl) scintillators (Tao 2012). On the other hand, CZT is able to offer considerable improvements in energy resolution which can be important to SPECT imaging (Iniewski 2014) and therefore the design choice was made to pursue the possibility of a CZT design rather than using scintillators and SiPMs.

The detectors chosen for the project are Redlen CZT detector modules (Redlen Technologies, Saanichton, BC). Each individual detector module is manufactured as a 2 $\times$ 2 array of bulk CZT substrate, where each substrate contains an 8 $\times$ 8 array of 2.46 mm pitch pixels. The substrates are bonded to a common cathode plate with individual pixelized anode plates creating 16 x 16 pixels per detector. The detector then includes an onboard application-specific integrated chip (ASIC) to process the events into a 256 event buffer on a field programmable gate array (FPGA) (Crestani 2010).

The architecture of each camera module was chosen to use four Redlen CZT detectors, resulting in a total of 32 x 32 pixels per camera. Each camera module then covers a

7.9 cm x 7.9 cm imaging plane. This selection was chosen as a trade off between a larger imaging area and the ability to have more cameras able to fit within the bore allowing for more projection angles. With a larger imaging area containing more pixels, the intrinsic resolution of the camera is improved and the possibility of a larger system FOV can be investigated. However for accurate reconstruction of the 3D SPECT image, more projections is desirable. With low numbers of projections, the images are more susceptible to artifacts and the tomographic resolution can suffer.

The footprint of the camera modules were also designed to allow for two modules to be placed adjacent to each other along the length of the bore, potentially creating a 7.9 cm x 15.8 cm imaging plane per camera. This would still allow for the same number of projection angles, but would give a larger field of view along the length of the bore.

3.3 Computer Hardware

The four CZT detector modules are controlled by a Teensy 4.0 microcontroller (600 MHz ARM Cortex-M7 processor, PJRC, Sherwood, Oregon). The microcontroller is used to poll the detectors for information such as operating temperature, change detector settings such as energy cutoff, begin and end acquisition, and read off the events stored in the detector modules' event buffers.

The microcontroller was selected because of its small footprint, fast communication speed capabilities, ease of programming, and its 600 MHz clock rate. As discussed in chapter 2, the EMI from electronics within the bore can be detrimental to MRI performance. By choosing a microcontroller with a clock speed well above the MRI operating rate of 128 MHz, the EMI given off by the clock pulse could potentially have a reduced effect on the MR image quality. The microcontroller then communicates back to a master computer located outside of MRI bore which sends commands to the system and processes the acquisition data for viewing. Methods of communication back to the

master PC computer were compared and will be discussed further. A standard laptop running a custom MATLAB graphical user interface (GUI) was used as the master PC for controlling the system during testing.

3.4 Printed Circuit Board Design

A custom printed circuit board (PCB) was designed for communication and power distribution. The PCB traces allow for the microcontroller to communicate with CZT modules using a master-slave protocol. Additionally, the PCB supplies the low and high voltage power to the microcontroller and the detector modules. The PCB uses two 20-pin header connectors and a high-voltage pin to attach the detector modules and a 26 pin header to attach the microcontroller. As with all the hardware components of the project, the connectors were chosen to have low magnetic susceptibility for mutual compatibility within the MRI environment.

High-speed serial peripheral interface (SPI) communication between the microcontroller and the four CZT detector modules was implemented using a low voltage differential signaling (LVDS) interface. This allows for reduced noise from the PCB during operation by (1) using lower voltages in each line and (2) causing the emitted EMI to have equal and opposite electromagnetic fields being produced by each trace. The destructive interference of the opposing traces work to cancel each other out reducing the noise given off. Additionally, LVDS is less susceptible to incoming EMI exposure due to the differential comparison which cancels out noise in the lines if it is present and equal in both traces.

The master-slave protocol between the master microcontroller and slave detectors works by polling the detectors individually, having them only respond when queried. Selection of the detector modules uses multiplexer switching. Due to limitations of the PCB design, the communication used a clock speed of 15 MHz, however the detector

modules are capable of running at up to 24 MHz. Separate from the main communication lines, the PCB also includes dedicated Reset, and Power-OK traces for each CZT detector which are used for startup and monitoring. An additional set of communication lines called the Event Flags are used during acquisition. These lines supersede the master-slave protocol and directly tell the microcontroller when an event has occurred in the corresponding detector.

A high voltage power supply and a low voltage power supply were used to provide DC power to the camera. Shielded power cables connected the power supplies (located at the edge of the MRI room) to the camera (located within the MRI bore). Ferrite chokes and BNC connector filters for low pass filtering were tested on the cables but were deemed unnecessary and a safety hazard in the MRI room due to their high magnetic susceptibility. The power traces on the PCB supply the high voltage bias (-450 V) which is applied across the CZT substrate and distributes the various low voltage power (voltages achieved using voltage regulators) that is required to operate the detectors modules (digital: 1.2 V, 2.5 V, 3.3 V, and analogue: 3.3 V, 5 V). Separated digital and analogue ground planes were used to reduce noise and ground loops. Passive low-pass filters were used on all power traces to reduce potentially harmful noise on the DC signal.

In order to keep the camera as flat as possible, all functionalities were implemented onto a single Board. The geometry of the PCB was designed to have the detector modules and microcontroller directly insert into pins on the surface of the board. The modules and microcontroller are easily removable from the camera for trouble shooting, repair, and future hardware changes. A second, smaller PCB was also designed to be placed on the microcontroller to allow for direct fibre optic communication. The PCBs were designed using EAGLE software and manufactured by OSHPARK. A board view and schematic view of the PCB is shown in (Fig. 3.1) and (Fig. 3.2).

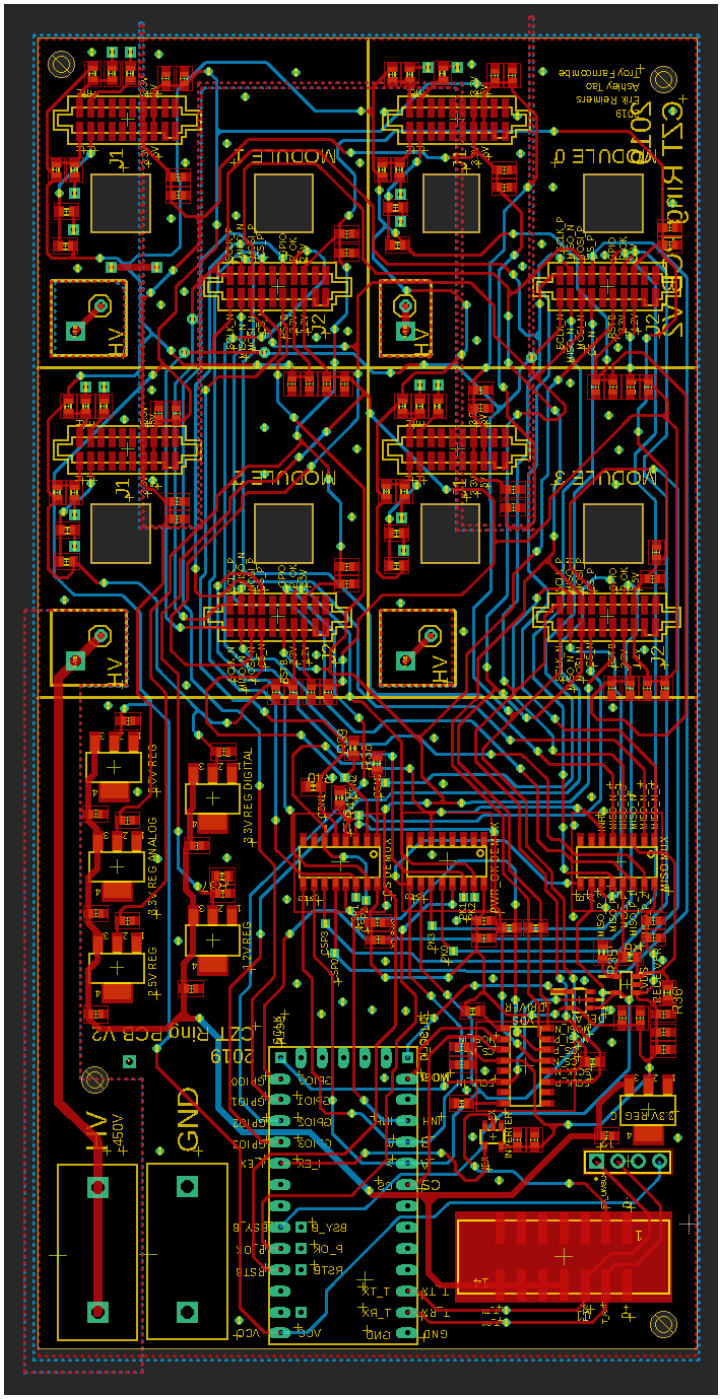

Figure 3.1: Gamma camera PCB board view design shown in EAGLE.

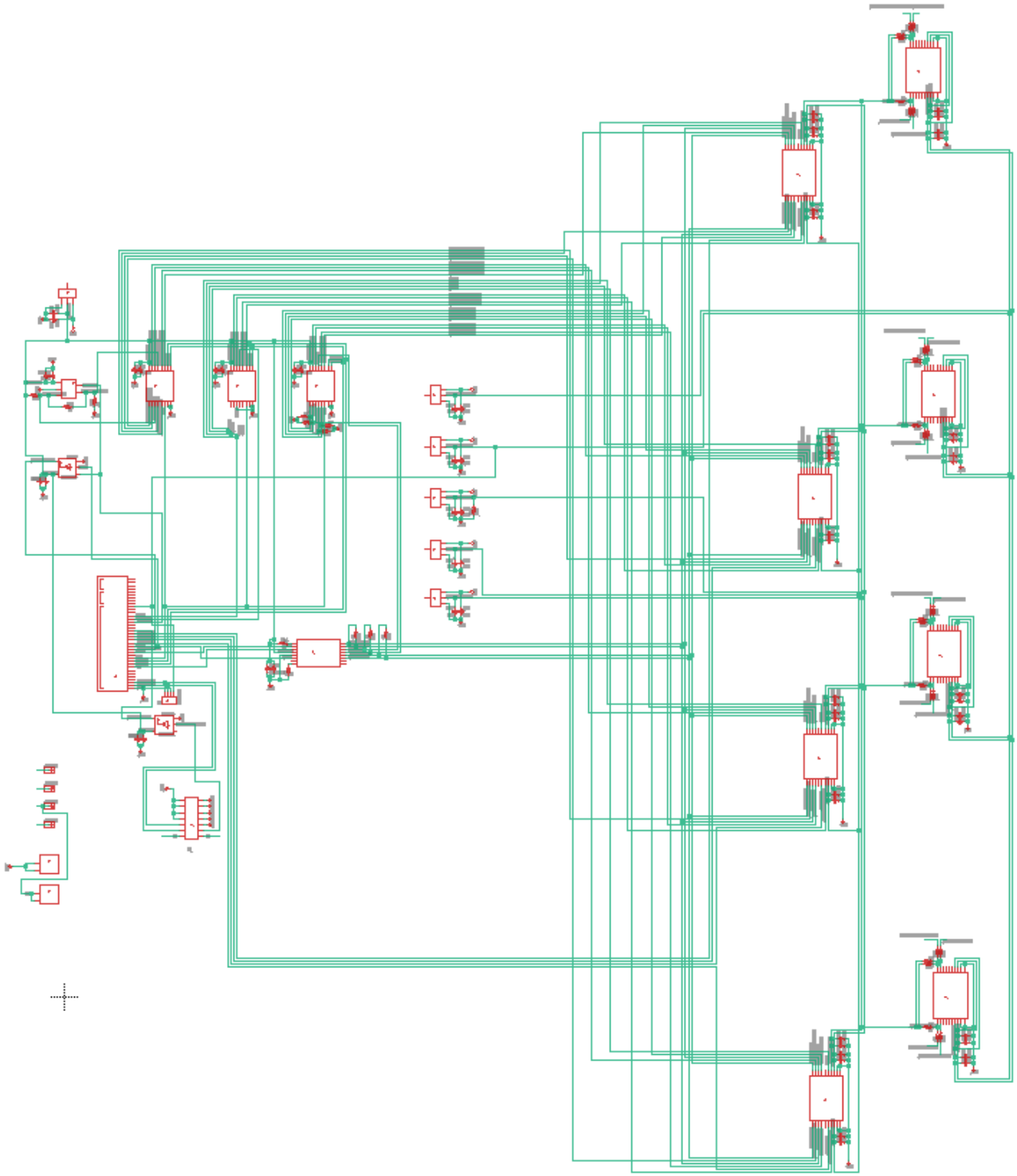

Figure 3.2: Gamma camera PCB schematic view shown in EAGLE.

3.5 Acquisition and Data Storage

In order to acquire event data, the CZT modules are put into Event Readout mode. Once initiated, each CZT module will acquire detected event data into an internal 256 event first-in-first-out (FIFO) buffer. Each event is stored as a 24 bit value (called an event frame) consisting of the detected pixel number (8 bits for pixel location describing the 16 x 16 pixels), energy channel (12 bits describing the analogue to digital converter bin number) and 4 addition bits (busy bit, error correction bit, event bit, and parity bit). During acquisition, the CZT modules will set their event flag pin high if there are currently events stored in their FIFO, and will continue to acquire and fill the FIFO further. The microcontroller constantly checks these flag pins in a round-robin fashion, where each detector has its events read out sequentially, emptying the FIFO, and restarting the process. If a FIFO fills before the event data is able to be read out, overwriting occurs and event information is lost. An Event FIFO Overrun indication bit is then set high and indicates the limit for the maximum count rate that the system is capable of achieving.

Previous testing done by A. Tao had used a Universal Serial Bus (USB) 2.0 communication line, which traveled from the microcontroller within the bore, to a master PC computer located in the MRI control room. This line was used to send operating instructions to the camera and also used during acquisition to send event data for each recorded event back to the master PC in live time. It was proposed that this current method may be giving off undesirable EMI, degrading the MR image quality. Instead, a new design was implemented to save the event data within the internal memory of the microcontroller either in flash memory or on a microSD memory card. Preliminary testing was performed of both options for their ability to store data within the MR environment. Both showed reliable performance, with no corruption of stored memory. However, the flash memory option was chosen due to hardware availability.

The 24 bit event frames are then sent to the microcontroller after detection. The microcontroller extracts the 8 bit pixel location information and the 12 bit energy information from the event frame. In addition to the 8 bit pixel location, a further 2 bits are added describing which of the four detectors the event was received from. This 10 bit location number now corresponds to the entire 1024 (32 x 32) pixel array of the camera. Due to memory limitations, the 12 bit energy value is truncated removing the four least significant bits. The new 8 bit energy value now describes 256 energy bins. The data is then stored in a 1024 x 256 array, which is the largest size possible with the memory limitations of the Teensy 4.0 microcontroller. The array allows for 1024 pixel bins (which matches the 32 x 32 pixels found on a single gamma camera module), and 256 energy bins. As the event data is received, the corresponding energy and pixel location in the array is incremented by 1 for each event. After acquisition has finished, this array is sent to the master PC computer which further processes the data array (such as photopeak selection) and produces a viewable image. A diagram summarizing the process of the data transfer from the CZT detectors to the viewable image is shown in Fig. 3.3. As of writing, the Teensy microcontroller 4.1 model has been released which still uses 600 MHz processing and offers microSD card memory. The additional memory will remove this memory limitation resulting in maximum energy resolution precision.

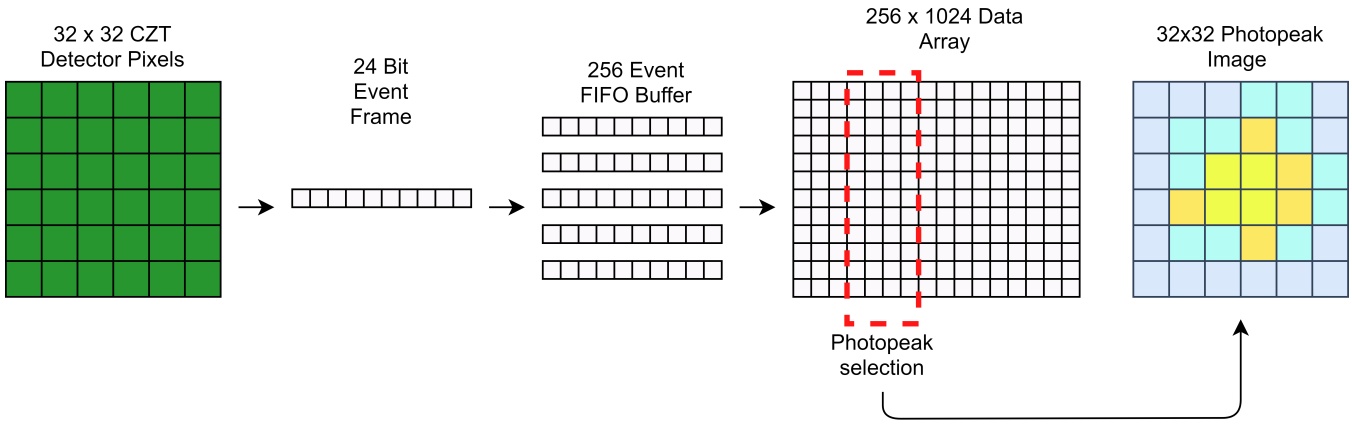

FIGURE 3.3: Diagram illustrating the process of the image data transfer. First the CZT detectors record an event location and energy. This information is processed into an event frame which is stored in its FIFO event buffer. The microcontroller then reads out the events stored in the FIFO and updates the data array to reflect the newly read events. Following aqusition, the data array is then sent to the master PC which selects the photopeak of interest and processes the events into a viewable image.

Because the energy bins are a unitless value taken from the detector's analogue to digital conversion process, they must be calibrated into an energy value. For initial proof of concept, the energy bins were calibrated using a linear fit from the energy peaks of two radiation sources: ^{99m}Tc and ^{57}Co. Ten 30 second acquisitions of each sources was acquired and the peak energy bin was recorded. The averaged peak energy bin for each source was used to create the linear fit using their known photon emission energies of 140.5 keV and 122.06 keV (Fig. 3.4).

Because the transfer of the array to the master PC is a slow process (∼20 seconds), a Fast Acquisition option was also implemented which does not use the data array method and instead individually saves each event frame up to a maximum of 128 events. This allows for quick viewing of an image for testing and trouble shooting. However for standard imaging, when the number of events stored in data increases by orders of magnitude, the data array method then becomes preferential.

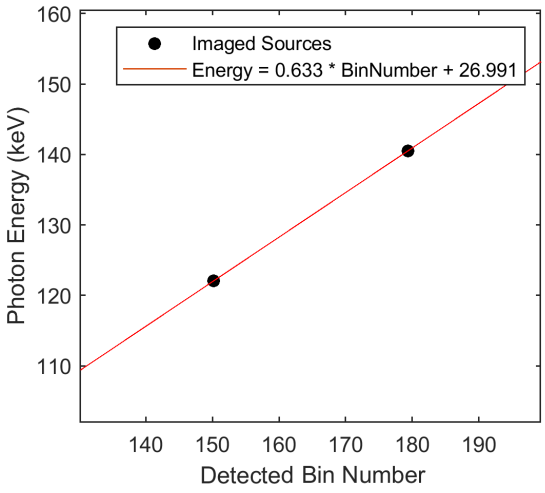

FIGURE 3.4: Calibration curve used for conversion of CZT detector energy bins to photon energy values. The two known energies of 140.5 keV for ^{99m}Tc and 122.06 keV for ^{57}Co were used.

Following acquisition, the detected event data is then sent back to a master PC located in the MR control room either via wireless 2.4 GHz Bluetooth or through an optical serial communication protocol. This process is performed after the acquisition has finished in order to limit further RF interference during the MRI sequence. However, if desired, the system is also capable of returning count rate information in real time during acquisition for additional insight into the temporal aspect of the mutual interference.

3.6 Teensy Software Development

The software for the Teensy microcontroller was programmed using the Arduino integrated development environment (IDE) with an additional package called Teensyduino. Teensyduino allows for integration compatibility between the Teensy and the Arduino IDE and offers several libraries for processes such as software interrupts.

The Teensy software is based off an optimized serial peripheral interface (SPI) library. This type of communication uses separate clock and data lines to synchronize

data transfer, along with a master-slave select line to choose which device of interest to communicate with. The library was customized by A. Tao to match the 24 bit frames specific to the detector modules used in the project. Using this library protocol, commands can be sent to the detectors and information and event data can be sent back to the microcontroller.

The Teensy is then controlled with a master PC which is located outside of the bore. The master PC features a MATLAB graphical user interface (GUI) which allows for easy access to all the control features of the camera from the MRI control room.

On power up of the camera system, the software first resets the detection modules using the dedicated Reset lines. After resetting, the modules will assert the Power-OK lines high, confirming functionality of each module. The software then waits for a user command in the form of a single operation number to proceed. The software allows for 14 operating procedures which are listed in Table 3.1. An overview of the functionalities of each mode is described below.

Table 3.1: Teensy Software Operating Procedures for The Gamma Camera System.

Operation Number	Operation Title
1	Write Register
2	Read Register
3	Read Pixel Map
4	Write Pixel Map
5	Fast Acquisition
6	Read Fast Acquisition Data from Teensy
7	Auto Disable Pixel Acquire
8	Camera Acquisition
9	Read Camera Acquisition Data from Teensy
10	Count Checker
11	Clear Bluetooth Buffer
12	Camera Acquisition V2
13	Reset
47	Bluetooth Connection

3.6.1 Write Register and Read Register

The Write Register and Read Register modes serve as the basis for communication with the CZT detection modules. The detection modules consist of multiple module registers, which are 8-bit blocks of memory that can be read and written to via the microcontroller master-slave SPI communication. Some registers consist of read-only memory such as the module serial number or the current operating temperature of the module. And others consist of read-write memory which can control aspects of operation such as the minimum energy detection cutoff or disabling specific pixels from operating. Sending the Teensy software into Write Register mode sends a 24 bit frame over the communication line to the desired detection modules. The frame includes the register address (which module register is to be written to) and the user's new register 8-bit data. This overwrites the registers and saves the new data into the detection modules. Read Register mode works in a similar fashion however instead of sending new data to overwrite, the detection modules return the current 8-bits stored in the register.

3.6.2 Read Pixel Map and Write Pixel Map

Throughout the testing of the detection modules, it was found that certain individual pixels of the CZT substrate were defective and could operate unpredictably. These faulty pixels made up $\sim$0.5% of the detector pixels and would report erroneously count rates, quickly filling the FIFO event buffer with false events before they can be read off. This then causes actual detected events to be lost due to overwriting. Because of this issue, it is common to require certain pixels to be disabled before normal operation can be achieved. The Read Pixel Map mode is used to read off the 1024 pixel states (whether the pixel is enabled or disabled) from the detection modules and send the information back to the master PC for analysis. The Write Pixel Map mode is then used to write an entire set 1024 pixel states to the detectors. Although it is unclear why, the pixels do not always maintain their pixel state. Therefore, it is necessary for the Write Pixel

Map mode to check each pixel and confirm that it matches the desired state. If the pixel does not match, the software will continue to rewrite the pixel's module register until the change has successfully been implemented.

3.6.3 Fast Acquisition, Read Fast Acquisition Data from Teensy, and Auto Disable Pixel Acquire

As discussed previously, instead of using the entire 1024 x 256 array to store the event data, it can be advantageous to store each event as a separate 32 bit value (the detector module number is combined into the 24 bit event frame) in a single list. With a low number of events, this makes reading off the data faster allowing for quicker trouble shooting of the system. The Fast Acquisition mode follows the same acquisition protocol that will be discussed later for the standard Camera Acquisition mode, however the data is stored in this compact manner. Additionally, the fast acquisition only lasts for either 3 seconds or up to 128 events. The Read Fast Acquisition Data mode is then used to send these events back to the master PC for quick analysis.

The faulty pixels which had to be disabled were found to not always be consistent and varied from test to test. To save trouble shooting time, an Auto Disable Pixel Acquire mode was created. The mode works when imaging background counts, which should result in a relatively even count rate across the detector. The software runs a Fast Acquisition (maximum of 128 counts) and checks whether a single pixel has reported more events than a specified threshold. If it has, it is considered faulty and is automatically disabled. Often, the faulty pixel will account for all 128 counts acquired. The process then repeats until the system has performed a specified number of "clean" acquisitions in a row, where no faulty pixels were found. Following the Auto Disable Pixel Acquire mode, the system is then ready for normal operation.

3.6.4 Camera Acquisition and Read Camera Acquisition Data from Teensy

The camera acquisition protocol uses a round-robin method, where each of the four detector modules are checked sequentially for potential events saved in their FIFO buffer. This process is shown in the flow chart below, (Fig. 3.5).

First the desired length of time for the acquisition is requested from the user. In the case of simultaneous imaging, the time length was approximately matched to the time length of the MRI sequence to provide maximum information on how the mutual compatibility effects were altering performance of each modality. An interrupt is used to trigger the Timer Flag when the acquisition time length has elapsed.

To begin acquisition, the data array for the events is first cleared to create a new image. The modules are then reset to clear any possible errors from previous runs, and finally they are put into Event Readout mode, which is what begins the acquisition process and the CZT detectors begin acquiring events.

The round-robin process then starts with the first module. Ensuring that the timer flag has not yet gone off, the module's Event Flag is checked. If the flag is low, the process moves onto the next module. If this flag is high, this means the module currently has one or more events saved in it's FIFO event buffer. These events are read from the module which clears the buffer. The events are then saved into data array. The software then returns back to the beginning of the round robin process. Once the Timer Flag has been triggered, the acquisition is complete. The modules are reset and put back into Register mode and the user is signaled that the process has finished.

Reading of the data from the microcontroller to master PC is then performed as a separate command with the Read Camera Acquisition Data from Teensy mode. This

Figure 3.5: Flowchart for the camera acquisition protocol.

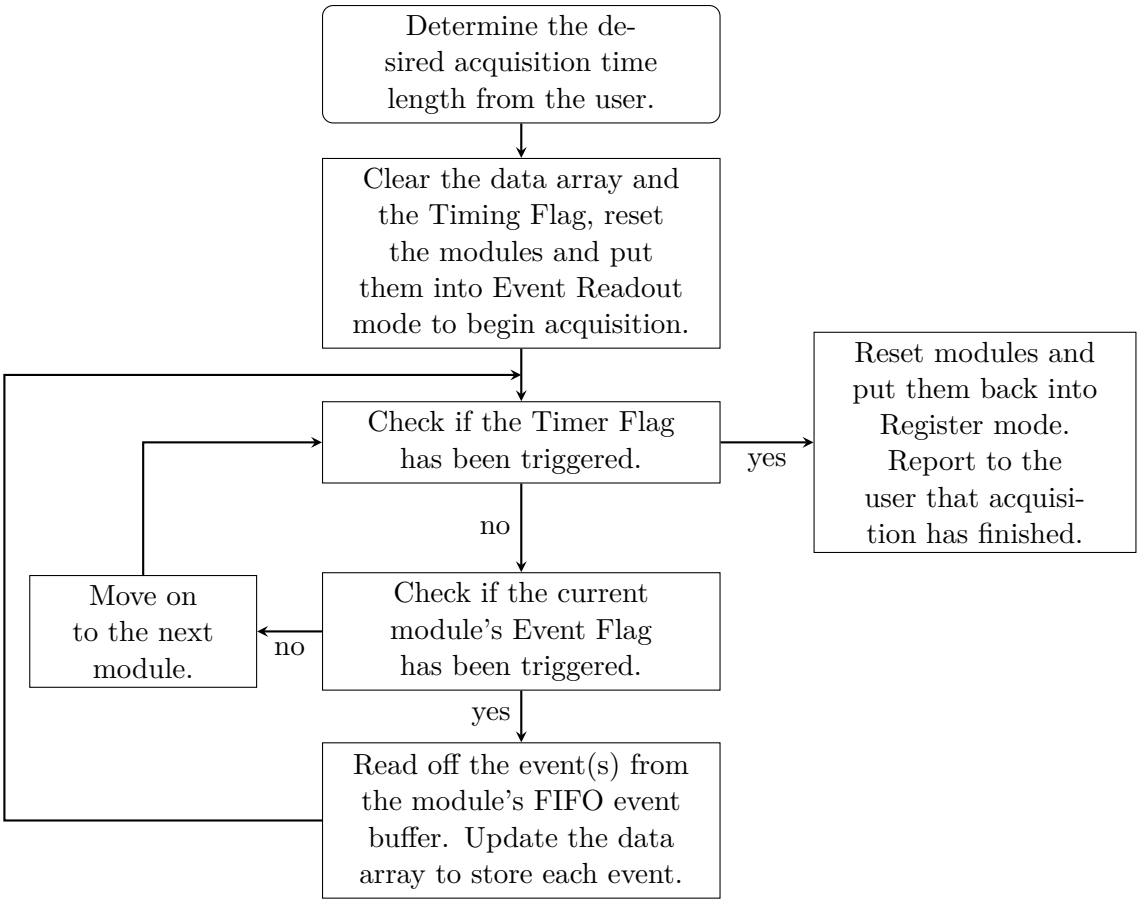

transfers the entire data array to the PC where it is then processed into an image for analysis.

3.6.5 Camera Acquisition V2

Camera Acquisition V2 takes the same protocol as discussed above, and adds an additional flag which is checked during the round robin process. A Gradient Triggering Flag is added which is set high whenever one of the three MRI gradients are in a switching phase. The concept of gradient triggering will be discussed further in Chapter 4.

During gradient switching it was determined that the CZT detectors should not be acquiring, as the events they acquire during this time are faulty and do not represent

the actual radiation distribution being imaged. By using the Gradient Triggering Flag, acquisition was programmed to pause during these short periods of time. Although taking the detector modules out of Event Readout mode does stop acquisition, this process was determined to be too slow as the gradient switching occurs over a period of several milliseconds. Instead, the detector modules still acquire during this time. However, following the gradient switching phase, the FIFO buffers are cleared without reading the erroneous events. This causes only the true events (which occur between gradient switching) to be saved into the data array.

Additionally, it was determined that the acquisition needed to be paused for an additional short period of time after gradient switching had finished. This was accomplished using an interrupt which is triggered when the Gradient Triggering Flag changes from high to low. The interrupt then starts a second software timer with its own timing flag. After this timing flag is triggered, the module event buffers are cleared and acquisition begins.

3.6.6 Count Checker, Clear Bluetooth Buffer, Reset, and Bluetooth Connection

Several additional commands were implemented for fast trouble shooting of the system. The Count Checker is used following an acquisition to tell the user how many counts saved during the last acquisition. This can be used before the slow process of sending over the data array in order to see if the last acquisition ran as expected. The Clear Bluetooth Buffer is used to clear the Teensy's serial buffer which can cause errors if the process of transferring data becomes interrupted. Reset is a dedicated mode for resetting the detector modules. And the Bluetooth Connection is used to confirm that the separate Bluetooth communication module is powered, connected, and operating at the same baud rate to the microcontroller's serial output. The value of 47 was used for

the Bluetooth Connection command because by default the Bluetooth module outputs a 47 value after success connection starting this command automatically.

3.7 Master PC Software Development

A MATLAB GUI (Fig. 3.6) was developed to run on the master PC, allowing for control of the Teensy located inside the MRI bore from the control room. The GUI features control of all the operation commands listed in Table 3.1, and processes the event data array or list into a viewable image. The main GUI displays three figures which show: (1) the gamma camera's acquisition image, (2) a histogram of the energy spectrum for the image, and (3) an optional counts-per-millisecond graph which updates as the image is being acquired. The GUI also contains the software used for image corrections. This includes: (1) energy windowing the image to only contain the energy range of interest, (2) applying a uniformity map to the image which takes into account the non-uniform sensitivity of the individual detector pixels, and (3) taking the blank pixels that were disabled prior to acquisition assigning them a value based on an average of the surrounding pixels. A second window of the GUI (Fig. 3.7) was developed for the pixel disabling/enabling.

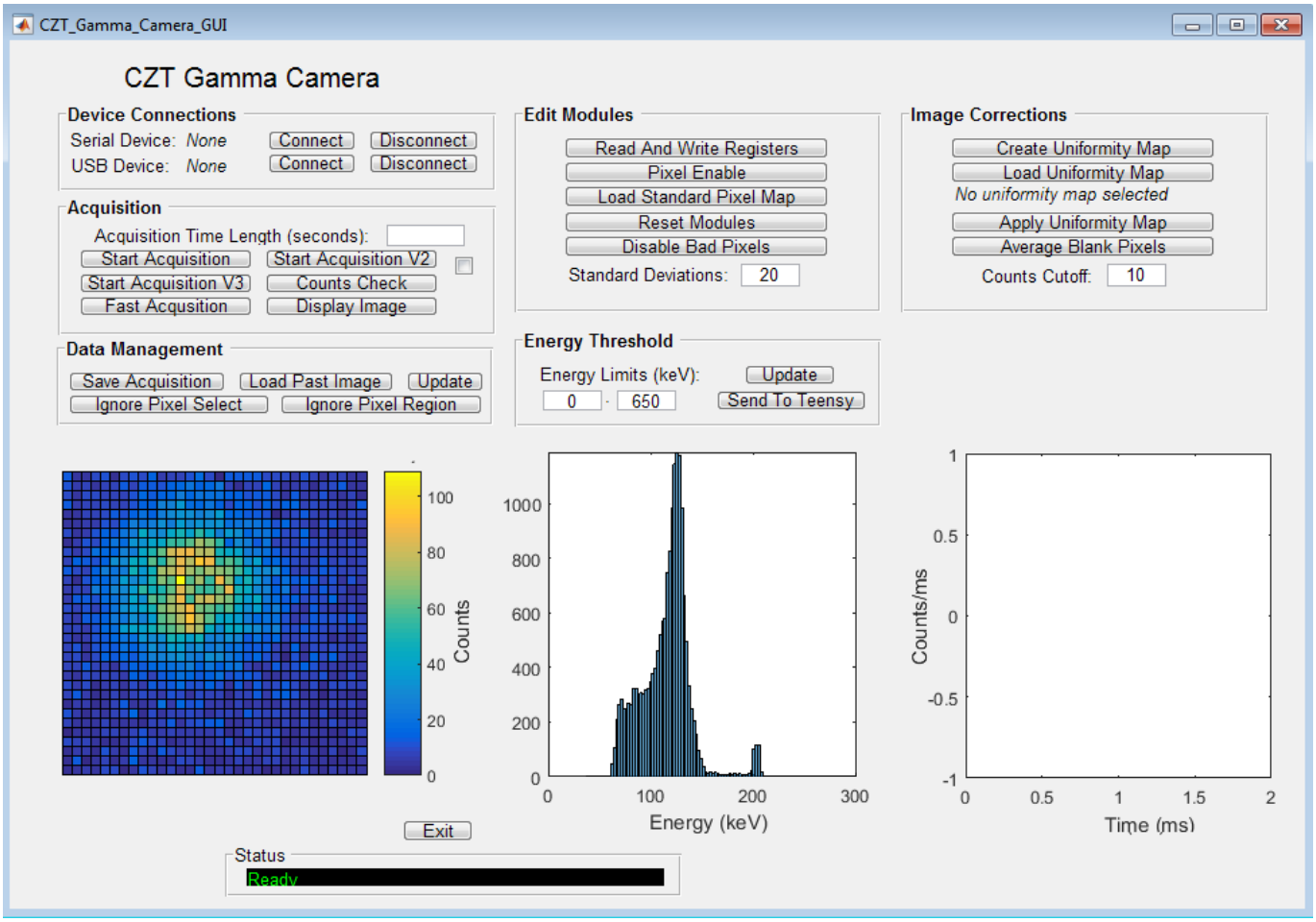

FIGURE 3.6: Main window of the MATLAB GUI used to the control the gamma camera module from the master PC.

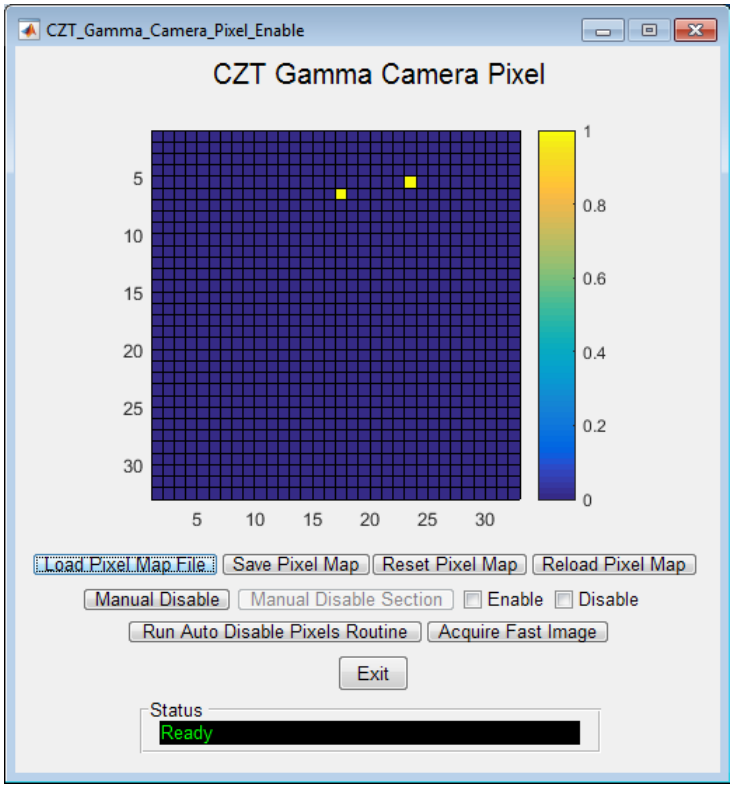

FIGURE 3.7: Secondary window of the MATLAB GUI used to control the pixel disabling and enabling features.

Chapter 4

Measurement of MR Gradient Effects in CZT Detectors Used in a SPECT/MRI System

Submitted in modified form to the 2020 IEEE Nuclear Science Symposium Medical Imaging Conference Record

4.1 Abstract

The first stage of testing towards the further development of a full-ring SPECT/MR system has been evaluated. Performance of the cadmium zinc telluride (CZT) detectors were found to be unaffected by the static magnetic field, however they were found to react unreliably during simultaneous imaging when the MR sequence repetition time (TR) was less than 400ms and were influenced significantly by the imaging gradients. In an effort to better understand this phenomenon, component testing was performed by subjecting the CZT detector modules and electronics to various gradient sequences in a stand-alone gradient testing apparatus.

We exposed the modules to 31 unique gradient sequence shapes of varying power and duration, typical of those used in clinical MR devices while simultaneously operating the CZT modules in event readout mode. Results indicate that certain detector pixels were preferentially affected (typically around the periphery of the detector array), leading to induced currents in the detector material and significant increases in erroneous event rates during the gradient ramp-up and ramp-down phases. The shape of the gradient waveform was also seen to have an effect on the detector performance with higher slew rates leading to impaired performance. Hardware disabling of the most severely affected pixels led to some reduction in erroneous background events, however, it also resulted in reduced detector resolution and sensitivity.

Subsequent work led to the development of a gradient triggering circuit to momentarily suspend CZT event detection during the MR gradient ramp up and ramp down intervals. Subsequent testing of this circuit in a clinical 3T MR was performed. When gradient triggering was enabled, erroneous event data was reduced to near zero levels and resultant images show no structural differences when compared to control acquisitions. During gradient application, the CZT modules are suspended, thus yielding a 60% drop in sensitivity due to the additional deadtime of the triggering. The produced MR image showed a reduction in SNR of 92%. Co-registration of the MR and gamma camera images was successfully performed, showing both the structural and activity makeup of the phantom.

4.2 Introduction

The current forefront of research in medical imaging technology includes working towards the combination of combining multiple imaging modalities into a single scan. Single photon emission computer tomography (SPECT) is an imaging modality that would benefit from a combined approach with magnetic resonance imaging (MRI) allowing for

improved anatomical reference of soft tissue regions. Such a system may have application in some cardiac, brain, breast, or theranostic applications (Yang 2018; Lai 2018). While positron emission tomography MRI (PET/MR) development has progressed significantly in the past decade, the same is not true of SPECT/MR. Difficulties in the design of such a system include the need for the SPECT system to be compact, stationary, unaffected by large magnetic fields (static field and dynamic gradients) and radio frequency (RF) pulses from the MRI, and to be contained to prevent its own electromagnetic interference (EMI). Previous work in our lab has focused on measuring the mutual compatibility of the individual components of a novel cadmium zinc telluride (CZT)-based detection system and on preliminary proof of principle (Tao 2016a). These initial results indicated that simultaneous imaging suffered from significant MR image artifacts and that CZT detector performance was severely degraded when using an MR repetition time (TR) less than 400 ms. Despite these artifacts, it provided a solid foundation to further study these effects and understand the influence of each MR component on the overall CZT detector system. Here we present further development of a CZT detector system with the ultimate goal of developing a stationary, full-ring SPECT system that can be inserted into an existing MRI bore for simultaneous SPECT/MR imaging.

4.3 Materials and Methods

We envision a full-ring SPECT system being made up of multiple individual gamma camera modules. These modules will then be placed in a ring that can be inserted into the MRI bore as a stationary insert. The design of each camera module uses solid state cadmium zinc telluride (CZT) detectors (Redlen Technologies, Saanichton, British Columbia). Each detector module consists of a 16 x 16 pixel CZT matrix along with associated ASIC detector electronics. A multiplexed 2 x 2 array of detector modules is controlled by a microcontroller (Teensy 4.0, PJRC, Sherwood, Oregon) situated on a custom printed circuit board (PCB). Each camera module comprises a 7.9cm x 7.9

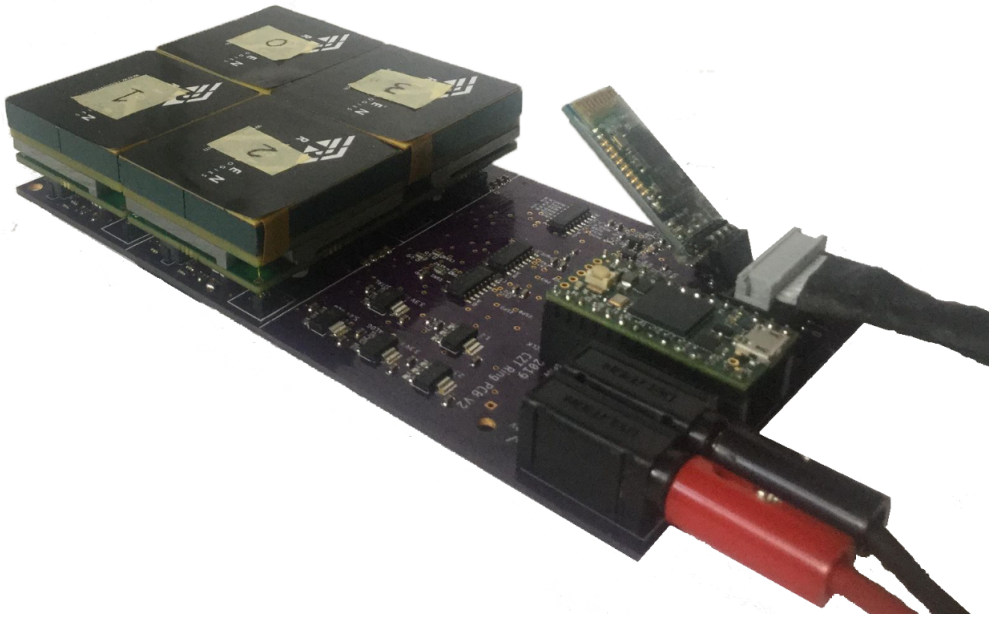

FIGURE 4.1: Single gamma camera module used for testing of mutual interference effects. The camera consists of four CZT detector modules, a PCB, a microcontroller, Bluetooth communication, and high and low voltage supply cables.

cm imaging plane. Once detection is initiated, the microcontroller communicates with each CZT detector module via high-speed differential serial peripheral interface (SPI) communication, storing each detected event in random access memory (RAM). Following acquisition, the detection data is then sent back to a master PC located in the MR control room either via wireless Bluetooth or through an optical serial communication.

Initial designs of this full-ring system have been simulated to evaluate the imaging characteristics of various collimator designs and are the subject of the next chapter. This research is being done to look into options for collimation design which would allow for: (1) a large enough field of view for a wide variety of applications, (2) a reasonable resolution-sensitivity tradeoff, and (3) keeping a small enough footprint to still fit within the MRI bore. In this work presented here, we evaluate the hardware viability of a single gamma camera module operating within the bore of a 3T MR system under simultaneous operation.

To investigate the mutual compatibility effects of the detector design, testing was performed with a 3T MRI (GE Discovery MR750), principally using a gradient echo sequence (GRE 3 mm thick, 24 cm FOV, 256 x 256 matrix, 30° flip angle, L/R phase encode direction, TE = 3.7 ms, TR = 14.2 ms). The camera module was placed within the bore next to a 32 channel receive-only head coil with a cylindrical water phantom used for imaging. The camera had high (-450V for CZT bias) and low voltage (6V for electronics) power lines extending out of the bore. Initial testing showed some noise present in the cables due to the operating MRI environment, however it was found that this noise was not significant enough to cause any malfunctioning from the system.

Bluetooth wireless communication was used to communicate between the master PC and the camera. For initial experiments, no radioactive source was used as the gamma camera was set to only acquire background counts in an unshielded and uncollimated configuration.

Subsequent work was performed to better understand the influence of the MR imaging gradients on CZT detector performance. This testing was performed using a custom gradient exposure coil (MRIdt, Western University) along with customized gradient sequences modeled on typical clinical acquisition sequences. The signal-to-noise ratio (SNR) of the MR image due to the SPECT system was determined and the effects of MR gradient shape, power and timing on the CZT detector electronics were investigated.

In order to reduce the influence of the MR imaging gradients on the CZT detector performance, we implemented a method to provide gated acquisition to the gamma camera module using gradient triggering. This was implemented using a custom differentiator circuit (Fig. 4.2) connected to the signal outputs (±5V) from the MR gradient power amplifiers. Each of the gradient output signals (x, y, and z gradients) is first sent through a high pass filter which selects for only periods of gradient switching. These signals are then passed through op-amp rectifier circuits and op-amp buffer circuits which forces a

positive signal regardless of whether the gradients are in a period of ramp up or ramp down. These outputs are then connected and sent through a comparator circuit with an adjustable reference voltage, forcing the analogue signal to be either logic high or logic low. The final result is a logic high when any of the MR gradients are in a switching state. This signal is then outputted to the gamma camera module via optical fibre cable to trigger acquisition via a Gradient Triggering Flag.

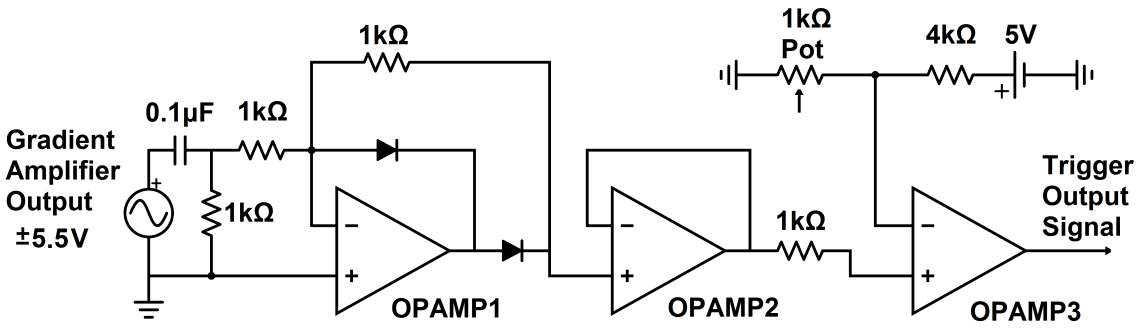

FIGURE 4.2: Schematic for the gradient triggering circuit. Circuit for only one of three gradient output signals is shown. The Gradient Amplifier Output is sent through a high-pass filter, a rectifier circuit (OPAMP1), a buffer circuit (OPAMP2), and a comparator circuit with an adjustable reference voltage (OPAMP3). The Trigger Output Signal is then set to the microcontroller to allow for gradient-triggered gated acquisition.

The camera was programmed to momentarily suspend its acquisition during times of gradient switching to eliminate the effects of mutual interference on the system. Further, to maximize the reliability of the system, an additional deadtime was added after the gradient switching had finished. This buffer was required to ensure the CZT detectors had returned to normal operation after the period of gradient switching.

To test the mutual compatibility effects while using the new gradient triggering protocol, the system was again placed in the 3T clinical MRI with a standard GRE sequence (GRE 3 mm thick, 24 cm FOV, 256 x 256 matrix, 5° flip angle, L/R phase encode direction, TE = 7.2 ms, TR = 50 ms). For better space maneuverability within the bore, a multi-purpose flex coil was used (NeoCoil 3.0T GEM Flex Coil). A non-radioactive

gelatin phantom (∼8 cm x 8 cm x 8 cm) containing four microcentrifuge vials of ^{99m}Tc pertechnetate was positioned within the coil. At the time of imaging, vials contained activities of 4.74 MBq, 12.6 MBq, 21.3 MBq, and 23.9MBq. The gamma camera was positioned ∼7 cm away from the edge of the phantom and imaged through the coil using a temporary low energy-high resolution parallel hole lead collimator. This collimator is not the final design collimator, but was deemed sufficient at this point to provide scintigraphic images to assess image quality.

An internal permit was obtained for the use of the radioactive ^{99m}Tc samples within the MRI room. The ^{99m}Tc was ordered by the nuclear medicine department at St. Joseph's Healthcare, Hamilton and the phantom was prepared in department's designated hot lab. The MRI room was temporarily designated as a basic nuclear lab with the appropriate signage posted for the duration of the experiment. Following the experiments, the protocol for decommissioning the room was followed.

4.4 Results and Discussion

Although no specific EMI shielding was used to shield the CZT detectors, they were immediately found to be sensitive to the MR room lighting and were therefore covered from exposure to the lights for all subsequent experiments.

Additionally, it was found that MRI sequences which used flip angles of greater than 30 degrees caused unreliability from the system as a whole. In particular, the microcontroller appeared to power off during the course of the MRI sequence. As this is the means of communication to the CZT detector modules, the exact effect on the detector modules from higher MRI flip angles is not known at this time. Although these higher flip angle sequences generally use higher power RF excitation pulses, The exact cause of this effect is not known and will be the subject of future research. As of now,

this limits the possible MR sequence to a gradient echo with a flip angle of 30 degrees or less.

The first area of investigation was the method of communication between the microcontroller and the master PC. It had been previously postulated by A. Tao that a Universal Serial Bus (USB) connection method may be resulting in high levels of EMI noise, leading to a degraded MR image. The camera was tested with and without the USB connection while simultaneously running an MRI acquisition (Fig. 4.3). During simultaneous imaging, horizontal line artifacts can be seen in the MR image. This is postulated to be due to the RF EMI from the camera electronics. The frequency encoding gradient creates a linear gradient of free induction decay frequencies across one dimension of the physical space. While the phase encoding gradient is applied in the other dimension of the slice. The MRI then uses its recieve coils to collect these frequencies. The lines are postulated to be certain EMI frequencies that are preferentially emitted by the electronics. This RF noise is collected by the MRI and manifests on the image as strong signals on certain frequencies and affecting all phases. Although care was taken to not have any components of the electronics operating at or near the MRI's standard operating frequencies of 128 MHz, it is possible that higher harmonics of a lower frequency from a source such as the SPI communication clock may be causing the artifacts.

When comparing the signal to background noise ratio (SNR), it was found that the MR image had comparable noise (SNR = 5.0) regardless of the USB connection in certain regions of interest (ROI) within the FOV, shown in the top row, (a). These are the areas where no differentiable line artifacts are apparent on the image. However in other ROIs, shown in the bottom row, (b), the USB connection causes its own strong line artifacts across the image degrading the MR image quality further (SNR of 2.5 drops to 1.6).

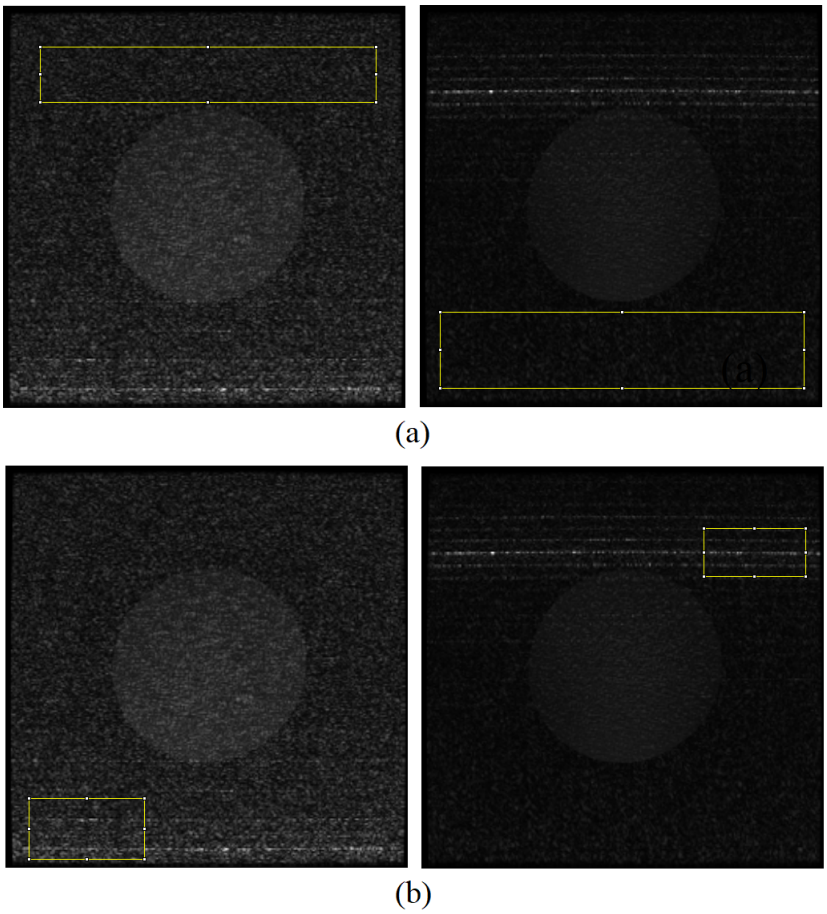

Figure 4.3: MR images showing the effects of a USB connection running into the MRI bore. Left: The system without USB. Right: The system with USB. The top row, (a), shows the ROIs which both result in an SNR of 5.0. The bottom row, (b), shows the ROIs which result in an SNR of 2.5 without the USB and 1.6 with the USB. Phase-encoding: L-R, frequency encoding: A-P.

This further reduction in image quality from the USB communication led to the investigation of an alternate method using a wireless Bluetooth module. Bluetooth operates at a frequency of 2.4 GHz, well above the MRI's 128 MHz operating frequency and was postulated to result in minimal interference.

Next the effect of microcontroller operating frequency was investigated. For comparison, a Teensy 3.5 microcontroller and a Teensy 4.0 microcontroller were powered but

running idle and positioned within the bore. The Teensy 3.5 has a processor clock speed of 120 MHz whereas the Teensy 4.0 uses a 600 MHz clock speed. The results showed that the clock speed of the microcontroller did have a strong effect on the MR background noise (Fig. 4.4). The Teensy 4.0 showed no significant difference from the control image, with a standard deviation (SD) of the noise of 68 for both tests. However, the Teensy 3.5 resulted in strong line artifacts and increased white-noise, with an SD of 315.

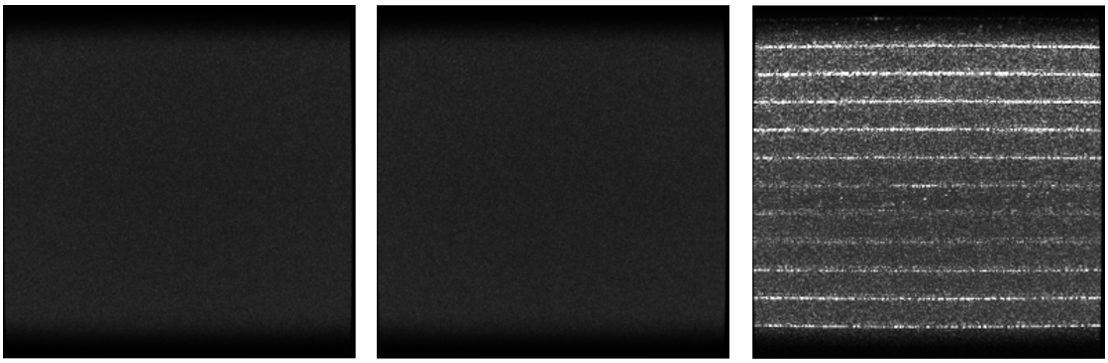

Figure 4.4: Resulting MR noise images comparing the effects of microcontroller processor clock frequency. (a) Control image with no microcontroller present, SD = 68. (b) Teensy 4.0 microcontroller operating at 600 MHz, SD = 68. (c) Teensy 3.5 microcontroller operating at 128 MHz, SD = 315. Phase-encoding: L-R, frequency encoding: A-P.

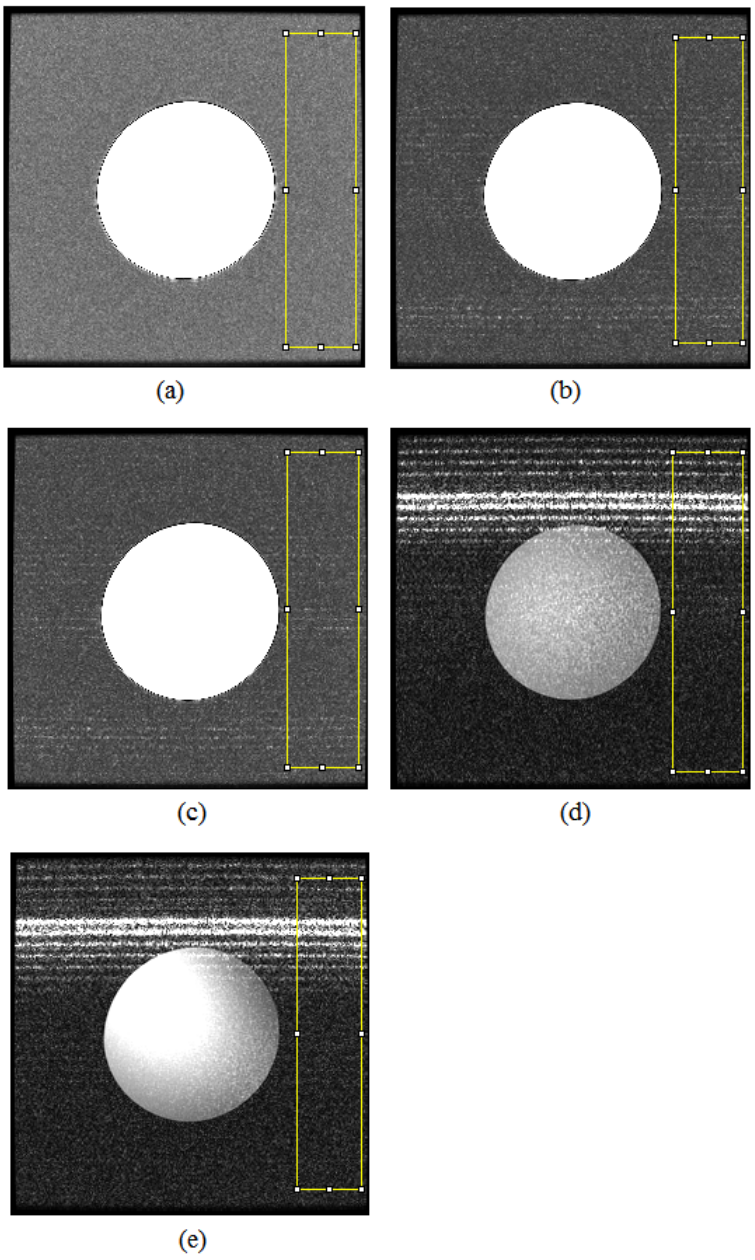

Figure 4.5: Resulting GRE MR images of a water phantom due to interference from a single gamma camera. Image contrast has been increased in order to see the subtle noise pattern. The regions of interest are shown for the SNR calculation. (a) Camera not powered. (b) Camera running idle. (c) Camera running with continuous Bluetooth communication. (d) Simultaneous imaging using four CZT detectors. (e) Simultaneous imaging using one CZT detector. Phase-encoding: L-R, frequency encoding: A-P.

Testing the effect of the new detection system on the MR performance showed that the presence of the unpowered camera module had no effect on the MR image (Fig. 4.5). However, a 50.4% decrease in the MRI signal to noise ratio (SNR) was found for a powered, yet idle detector module. A similar 51.9% decrease in SNR was observed while continuous Bluetooth communication was active. Finally, simultaneous SPECT/MR imaging led to a 99.4% SNR decrease.

During simultaneous imaging, comparable image degradation occurred regardless of the number of CZT detector modules used. It is therefore postulated that this increase in noise is due to RF EMI given off by the additional high-speed digital communication required to retrieve and store each detected event during acquisition rather than due to the CZT detection mechanism itself. This effect warrants further study, but we are hopeful that the addition of RF shielding of the digital electronics may reduce this effect significantly.

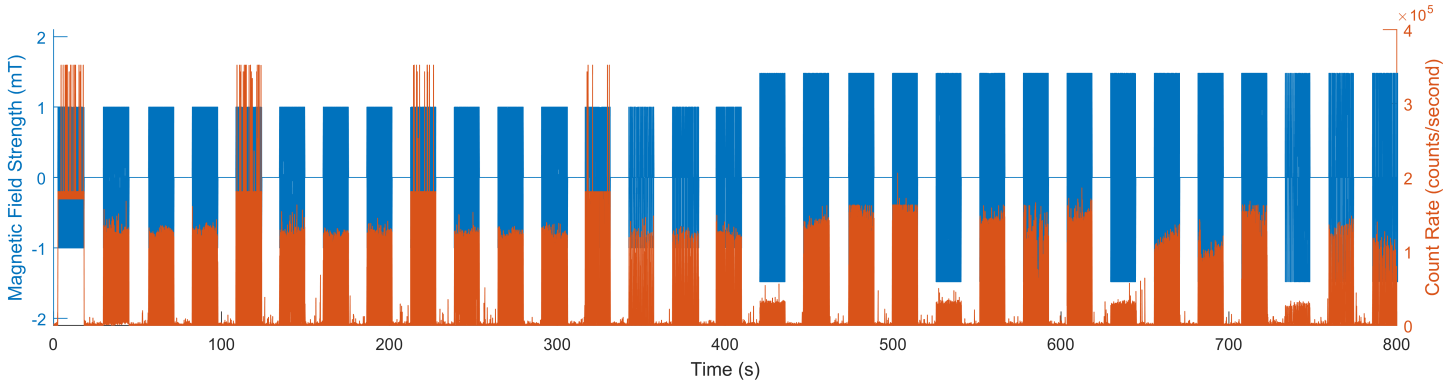

Figure 4.6: Count rate of the gamma camera (orange) when subjected to 31 unique gradient sequences (blue). Unexpected high count rates occur due to the presence of the gradient sequence.

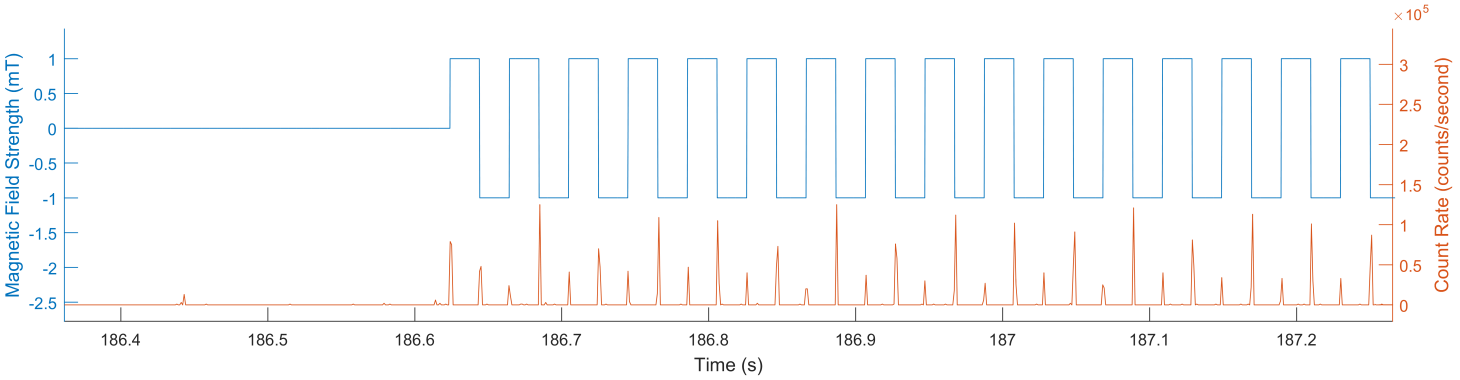

Figure 4.7: Count rate of the gamma camera (orange) when subjected to a gradient sequence (blue). Spikes in the count rate occur only during times of gradient ramp up/ramp down intervals.

Performance of the CZT detection system was found to be unaffected by the static 3T field. However, MR RF pulses and gradients were found to cause unreliable performance from the detectors when the GRE repetition time (TR) was lowered below 400ms. This manifested itself as a large increase in detected events over the entire detectable energy range and is surmised to be the effect of induced eddy currents within the analog detection chain. This large increase in detected counts quickly overwhelms the detection electronics, leading to a paralyzation of the detector system.

In order to further understand the source of this unwanted artifact, further investigation was performed by subjecting the SPECT system to gradient effects only at an MR device testing facility at Western University. The detector module and acquisition electronics system were subjected to 31 unique gradient sequence shapes of varying power and shape over the course of ∼15 minutes. The gradient waveform for each sequence was recorded in real-time along with the resultant gamma camera detected event rate in 0.1 ms intervals (Fig. 4.6). The parameters for each gradient waveform are listed in the appendix, Table A.1 with a diagram of the timing parameters shown in Fig. A.1. An example of the first two waveforms are shown in Fig. A.2 and Fig. A.3. No radioactive sources were used here as the study was used to determine the effect of the gradient fields

independently on the CZT detector performance. Hence, expected count rates should be low.

It was found that all sequences caused significantly higher (several orders of magnitude) than background count rates. However, sequences which used faster slew rates were found to be more detrimental than those with slower slew rates. Large increases in the CZT detector count rate directly correlated with application of the magnetic field gradient switching as determined from the gradient waveform (during ramp up/ramp down intervals) (Fig. 4.7). It is believed that the changing magnetic fields of the gradients induce currents in the detector material leading to the false events. These additional undesired counts were found to occur with reproducibility on specific pixels of the CZT pixel array, principally located around the periphery of the detector modules (Fig. 4.8). The exact mechanism responsible for this is still under investigation, but may be related to the skin effect due to the gradients. Hardware disabling of these pixels is possible, thereby resulting in more uniform image maps and reduced count rates even at gradient powers beyond that found in a clinical MRI system, but is undesirable as it results in a reduced active detection area and reduced sensitivity.

While it may be possible to reduce the influence of the gradient on the peripheral pixels through additional RF shielding, instead we investigated the use of a gradient trigger circuit to gate the gamma camera acquisition during gradient switching phases.

Testing of the triggering protocol showed reliable performance from the gamma camera during simultaneous imaging when the module was disabled during gradient application and with an additional trailing "off" time of 20 ms (Fig. 4.9). The produced images showed no structural differences when compared to control acquisitions taken without an MRI sequence running. However due to the additional deadtime from triggering, the total counts were 60% lower than the control.

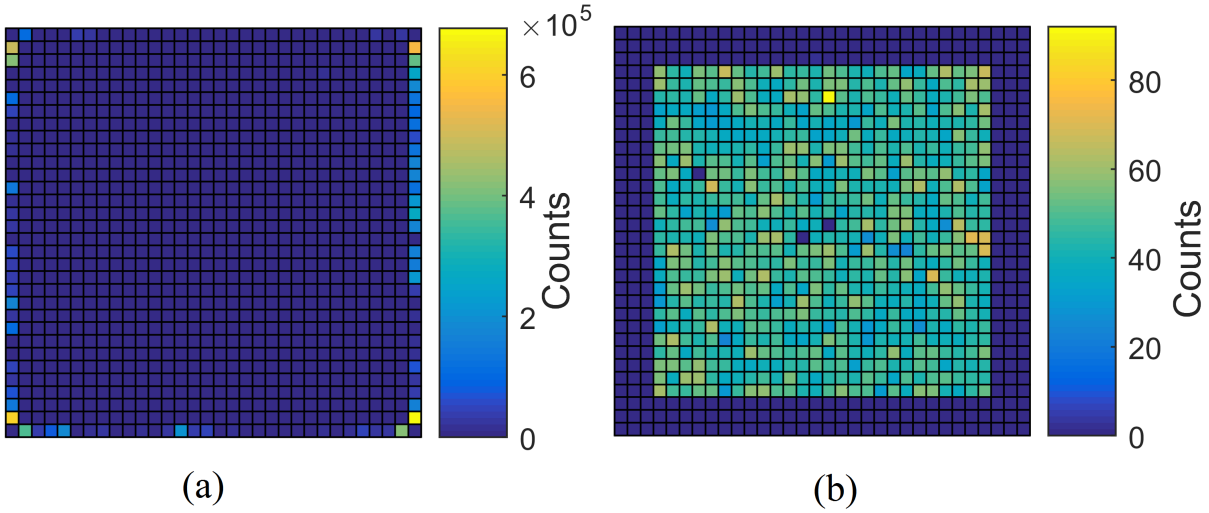

FIGURE 4.8: Gamma camera image (800 second acquisition time) of the 32x32 pixel gamma camera exposed to background radiation only during typical gradient sequence. (a) High event rate pixels are seen in the CZT periphery during gradient application. (b) Gamma camera image after the software disabling of affected peripheral pixels. The resultant image is much more uniform and has much lower and consistent event rates across the central 26x26 pixel area.

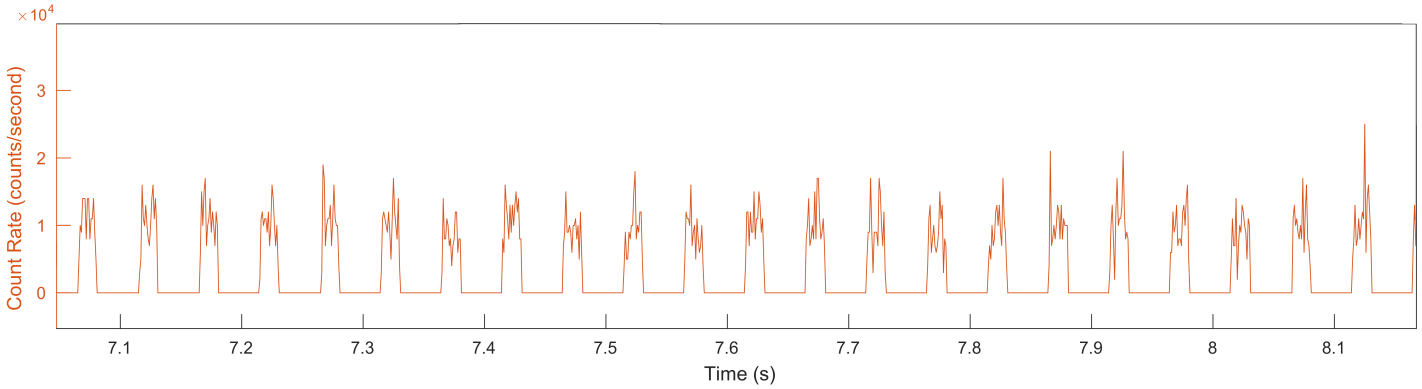

FIGURE 4.10: Count rate of the gamma camera (orange) during simultaneous acquisition with active gradient triggering being applied. Spikes in the count rate due to gradient switching have been suppressed with the true events being collected between times of switching.

A sample of the detector count rate over the course of a triggered simultaneous acquisition showed the successful suppression of the gradient induced spikes (Fig. 4.10)

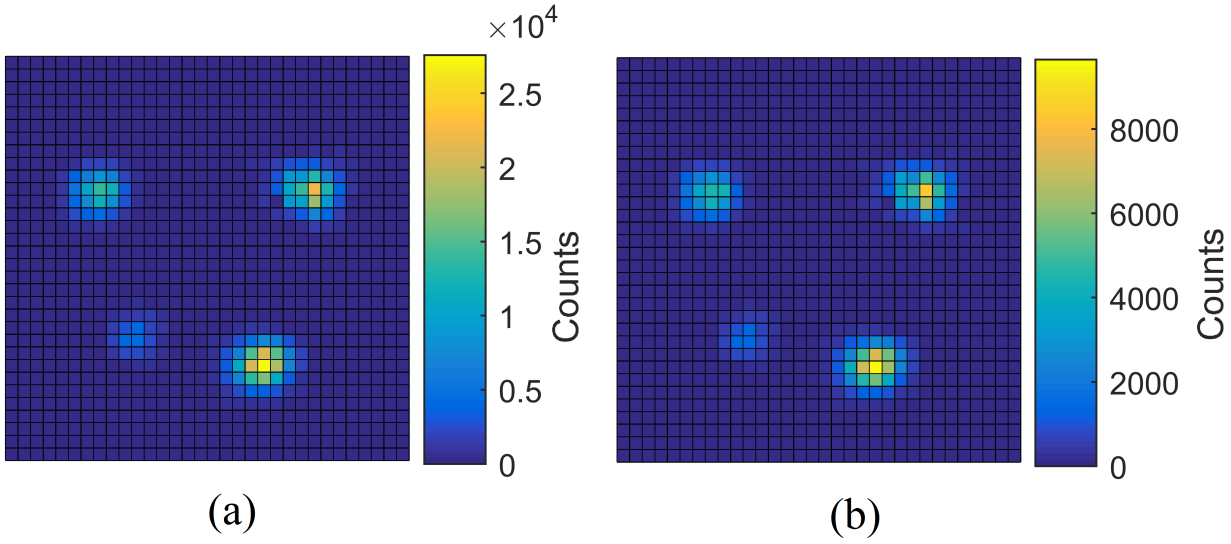

FIGURE 4.9: Gamma camera image (140 second acquisition time) of four ^{99m}Tc vials with varying activities. (a) Control image taken within the MR bore but without a sequence running. (b) Simultaneous imaging using the gradient triggering protocol.

compared to acquisitions when no gradient triggering was performed when the camera module acquired in excess of 100k counts per second. During times of gradient switching and the following associated buffer time, the detectors did not store events into memory resulting in no additional erroneous counts.

For this simultaneous acquisition test, an MRI repetition time (TR) of 50 ms was used. With a gradient switching time of ∼10 ms and an additional buffer of 20 ms there is a 60% deadtime which accurately matches the drop in total counts compared to the non-simultaneous acquisition when no gradient triggering is required. Although this reduction in sensitivity is considerable, a full ring SPECT system using this method is still expected to have comparable sensitivity to that of a standard rotating SPECT system due to the additional camera modules present.

When looking at the effects on the MR image, simultaneous imaging with gradient triggering was found to cause a 92% reduction in SNR (Fig. 4.11), similar to results

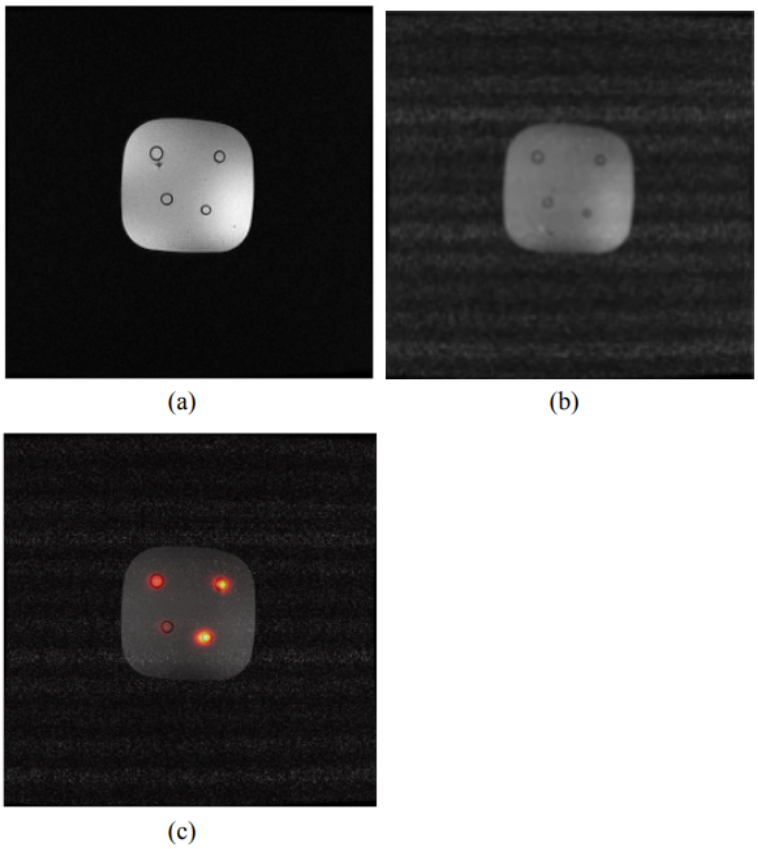

FIGURE 4.11: GRE MR image of the gelatin phantom containing four vials of ^{99m}Tc. (a) Control image taken with the gamma camera powered off. (b) Simultaneous imaging with the gamma camera. (c) Coregistration of the MR image with the simultaneously acquired gamma camera image.

determined previously. It is postulated that this RF noise is occurring due to high speed digital communication between the detector modules and the microcontroller as noise contribution appeared to correlate with the detected event rate. This effect will be the subject of further study and we are hopeful that the addition of RF shielding around the gamma camera modules may significantly improve the MR SNR. Despite the additional noise, co-registration of the two images was successfully performed using manual co-registration showing both the structural makeup of the phantom and the varying activity strengths of the four sources.

The energy spectra of the two gamma camera phantom images (sequentially acquired and simultaneously acquired) are shown in Fig. 4.12. The energy resolution of the system was calculated as the FWHM of the Gaussian fit of the photopeak. The FWHM was found to be 16.0 keV for sequential imaging and 17.0 keV for simultaneous imaging (at 140.5 keV). This corresponds to an energy resolution of 11.4% and 12.1% respectively. Because a process of truncating the energy bits was performed to save memory, this may not accurately represent what the system is capable of achieving. However, because the least significant bits were truncated, it should still give an approximate measure of the energy resolution.

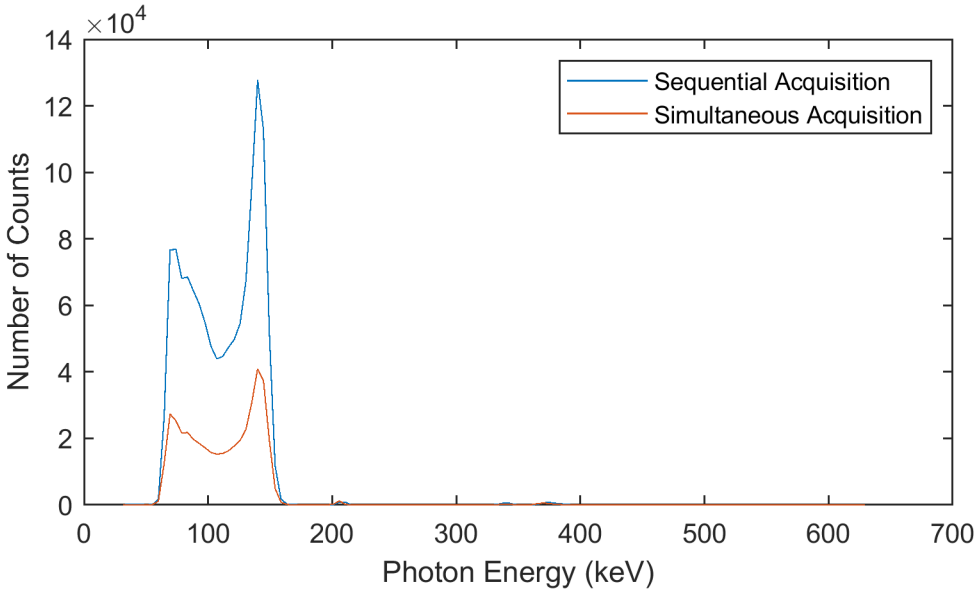

FIGURE 4.12: Energy spectra for the sequential and simultaneous acquisitions. Respective energy resolutions of 11.4% and 12.1% were found for the two spectra.

4.5 Conclusions

We have tested the impact of MR switching gradients on CZT detector performance. Without compensation, application of MR gradients leads to significant background detection rates, quickly overwhelming true detected counts. Using a gradient testing

facility, we were able to determine that increases in detector count rate occur primarily during the gradient ramp-up and ramp-down phases. Based on these observations, we have implemented a gradient triggering circuit coupled to the MR gradient amplifiers, in order to suspend acquisitions during the gradient switching intervals.

With this triggered acquisition, erroneous detected counts have been eliminated from the CZT data acquisition, albeit, with a 60% reduction in detection sensitivity due to additional dead-time during the gradient application. We have measured reductions in the MR SNR of around 99% when acquiring photon data. Through improved EMI shielding, disabling faulty pixels, and/or precise acquisition timing between gradient switching, we believe many of these effects can be reduced and that a full scale CZT detector system could be viable.

Chapter 5

Monte Carlo Simulation of Diverging Collimator Geometries for Full Ring Simultaneous SPECT/MR

Submitted in modified form to the 2020 IEEE Nuclear Science Symposium Medical Imaging Conference Record

5.1 Abstract

The potential of a diverging fan beam collimator for use in a multimodal SPECT-MR system has been investigated. Collimation was designed for use with a stationary ring of gamma camera modules each comprised of a 32 x 32 pixel CZT detector. The collimators provide a desired field of view (FOV) of 25.0 cm at the center of the bore. Eleven collimator designs were compared, yielding between 13 to 23 modules per ring. Each design was evaluated using reconstructed resolution and sensitivity metrics. The designs were simulated with the Monte Carlo software, GEANT4 Application for the

Tomographic Emission (GATE) and tomographic reconstruction was performed with a maximum-likelihood expectation maximization (ML-EM) algorithm in MATLAB. The results showed that a practical SPECT/MR design using 18 detectors per ring with a 3.83 cm length collimator gave equivalent tomographic resolution to that of a clinical SPECT/CT system but with 7.0 times greater detection sensitivity compared to the conventional rotating dual-head camera. Resolution across the reconstructed 25 cm x 25 cm FOV did show slight non-uniformity, with resolution improving around the periphery of the FOV as much as two-fold. A smearing artifact was seen in the corners of the FOV likely due to undersampling within those regions. A reconstructed hot-rod resolution phantom matched the previous results, giving similar resolution performance. However, the simulation also showed that the system suffers from aliasing effects when reconstructing features of 7.9 mm or less. To further investigate how the design choices affected the tomographic resolution, parameters for collimator hole size, detector pixel size, and number of projection angles were explored. Both the reduction of hole size and pixel size each allowed for improved resolvability down to 7.9 mm and 6.4 mm respectively. Increasing the number of projection angles was found to remove smearing artifacts from the image, however it did not significantly change the resolution. The resolution is therefore believed to be limited by the 2.46 mm pixel size and associated pixel matched collimator. These are promising results that show that a diverging fan beam collimator could be a viable choice for a SPECT/MR system.

5.2 Introduction

Among the expanding selection of multimodal medical imaging techniques, SPECT is an imaging modality that could potentially benefit from a combined system with MRI. When compared to the current standard of SPECT/CT, a combined SPECT/MR system would allow for improved anatomical contrast of tissue regions such as brain or soft tissue. A system such as this may have application in some cardiac, brain, breast or theranostic

applications (Yang 2018; Lai 2018).

However, the development of a SPECT/MR system is lagging behind other similar modalities such as PET/MR. One challenge faced by SPECT/MR which is not found in PET/MR is the requirement of photon collimation within the system, requiring discrete projection sampling. In comparison to current clinical SPECT/CT systems, SPECT/MR requires novel collimator design due to space constraints and the use of non-traditional detectors. Additionally, the requirement to acquire projection data around the entire patient traditionally demands that clinical systems physically rotate, thus presenting further impediments to development of a SPECT/MR device (Audenhaege 2015). Because of the limitations of current clinical designs, we have considered a new full-ring SPECT design. Here we present simulation results of full-ring, diverging collimator geometries for SPECT. These collimators are specifically for use with a full-ring SPECT system made up of multiple gamma camera modules. These camera modules are currently in development and will fit inside an existing MRI bore as a ring insert, allowing for simultaneous SPECT/MR imaging.

5.3 Materials and Methods

We have modeled our simulated SPECT systems on a pixelated solid-state cadmium zinc telluride (CZT) detector developed by Redlen Technologies (Saanichton, British Columbia). Each detector module consists of a 16x16 pixel (2.46 mm x 2.46 mm) CZT matrix along with associated ASIC detector electronics. A camera module utilizes a 2 x 2 array of the aforementioned CZT detectors situated on a custom printed circuit board (PCB). The dimensions of each gamma camera module (not including collimator) is 7.9 cm x 7.9 cm x 2.8 cm.

Following a similar design to that of current clinical PET/MR systems, the SPECT camera modules are placed directly around the periphery of a 70 cm MRI bore as a

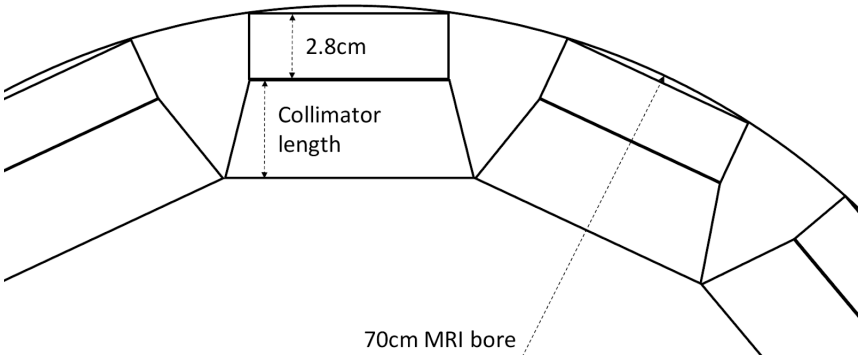

FIGURE 5.1: Partial diagram of stationary detector ring which fits into a 70 cm MRI bore. The detector and associated electronics length of 2.8 cm is shown. The collimator length was varied for each simulation run.

ring insert (Fig. 5.1). Although increased distance from the imaging region generally lowers resolution, this design maximizes space within the bore for the patient, reducing the chance of claustrophobia (Muzic Jr. 2014). Testing of the camera hardware was performed using a 60 cm MRI bore, however the final design would be built for a 70 cm MRI bore.

While other full-ring SPECT systems have made use of pinhole and slit-slat collimation (Cai 2013b; Meier 2011; Salvado 2014), it was thought that these systems take up valuable space within the bore and tend to offer low sensitivity Audenhaege 2015. With this space constraint in mind, the option of a diverging fan beam collimator geometry was investigated with a diverging geometry in the x-y plane and a parallel hole geometry along the z-axis. Given a desired 25.0 cm field of view (FOV) and the fixed 7.9 cm camera size, a focal length of -14.7 cm was selected in the diverging direction. The collimator used square holes with a 1:1 pixel matched design, having each hole directly aligned with a detector pixel. This allows each pixel to act independently offering improved spatial resolution and sensitivity over traditional hexagonal hole designs (Mueller 2003). All geometries used lead as the collimator material with 0.2 mm septal thickness as both of these parameters have shown promising results in past hardware compatibility testing (Tao 2016a) and would be comparable with low energy, high resolution parallel hole

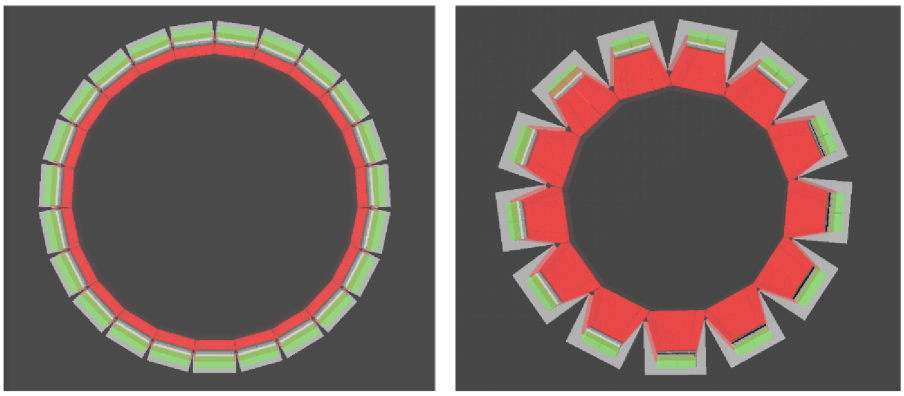

FIGURE 5.2: 3D representation of the GATE simulation for the SPECT detector ring. Detectors and associated electronics are shown in green with the collimators shown in red. Changes in collimator length leads to a different number of camera modules fitting into the MRI bore. (a) 1.13 cm collimator with ring of 23 cameras. (b) 7.67 cm collimator with ring of 13 cameras.

collimation.

Variation of the collimator length results in a resolution-sensitivity trade off. Additionally, collimator length also determines the number of camera modules that are able to fit within the MRI bore (Fig. 5.2), thus leading to fewer projection angles. This additional trade off can also affect system performance.

The lengths of the collimators were maximized for each ring geometry to fit flush against the adjacent collimators, allowing for optimized use of the limited space within the bore. Eleven collimator options were compared, which corresponded to rings of between 13 to 23 cameras. The collimator lengths which correspond to the desired number of camera modules were calculated using equation 5.1 (derived from the relation between the side length of a regular polygon to its interior radius). Where L is the collimator length, d is the diameter of the MRI bore, W is the width of the camera module, h is the height of the electronics and detectors, N is the number of cameras, and f is the focal length. The simulated geometries are listed in Table 5.1.

$$Ł = \frac{f \cdot tan(\pi/N)(\sqrt{d^2 - w^2} - 2h) - f \cdot W}{2f \cdot tan(\pi/N) - W} \tag{5.1}$$

TABLE 5.1: Collimator Lengths For SPECT Ring Geometries.

Number of Camera Modules in Ring	Length of Collimator (cm)
13	7.67
14	6.78
15	5.96
16	5.20
17	4.49
18	3.83
19	3.22
20	2.65
21	2.12
22	1.61
23	1.13

These geometries were modeled using GEANT4 Application for the Tomographic Emission (GATE). Models for the full width at half maximum (FWHM) of each collimator design were empirically determined for both the diverging and parallel directions by using a small point source of Tc-99m and positioning this source at a variety of distances from the camera surface. These collimator models were then used to develop a custom, iterative, ML-EM, tomographic reconstruction algorithm in MATLAB that takes into account the 3D detector resolution effects and layout of the ring.

The ML-EM algorithm uses the FWHM models to create a system probability matrix which maps the probability that a given voxel is seen by a given pixel, and vice versa. This is done for every pixel in the ring and for a single center slice of the imaged voxel space. Using an iterative procedure, an initial estimate of the source distribution is updated through a comparison correction term for a specified number of iterations. For 3D reconstruction of multiple voxel slices, the algorithm cycles through each slice by making the current slice act as the center slice. This is done by shifting the projection images either up or down and reusing the same system probability matrix. Each slice

can then be updated during each iteration. This method of shifting the image (rather than having a unique probability matrix for each slice) was used to save computational memory.

To test for tomographic resolution and sensitivity, a 1.0 MBq 99mTc point source was placed in the center of the FOV and simulated for a 120 second period. The reconstruction was performed using 100 iterations and the resulting image was analyzed for spatial resolution by determining the FWHM of the reconstructed point source. Sensitivity was calculated using the total number of counts detected over the acquisition time period. Resolution of the reconstructed image across the entire FOV was also investigated using the 18 camera geometry. A GATE simulation for a 3D grid of 15 point sources was reconstructed using the 3D multi-slice method and an analytical simulation of a hot-rod resolution phantom using standard rod sizes (diameters of 4.8, 6.4, 7.9, 9.5, 11.1 and 12.7 mm) was evaluated to investigate this.

Next, alternative design options were compared to see if performance could be improved further. Using the 18 camera hot-rod phantom result as the control image, design parameters for the collimators and detectors were independently altered and the resulting change in tomographic resolution is presented here. (1) First the effect of using smaller collimator holes was investigated. Rather than a 1:1 pixel-matched geometry, a 1:4 pixel matched collimator was implemented, where four collimator holes are used per CZT pixel. Although this design results in a lower sensitivity, it may show the possible limits of resolution capable from the current detectors. (2) Next a hypothetical CZT detector with a smaller pixel size was investigated to see how the pixel size limits performance. A detector with pixel density increased by a factor of four (now 64x64 pixels per camera module) with a corresponding 1:1 pixel-matched detector was used. (3) Finally, the effect of having limited projection angles was investigated. Partial rotations of the ring were simulated to give 18, 36, and 54 unique projection angles for reconstruction

of the designs mentioned above. The parameters for the analytical hot-rod phantom simulations are summarized in Table 5.2.

.

Table 5.2: Collimator Summary Of Parameters For Hot-Rod Phantom Comparisons.

Detector-Collimator geometry	Number of projection angles
2.46 mm pixels with 1:1 pixel matched collimator	18, 36, 54
2.46 mm pixels with 4:1 pixel matched collimator	18, 36, 54
1.23 mm pixels with 1:1 pixel matched collimator	18, 36, 54

For selection of a potential geometry moving forward with the project, these results were compared to the reported system specification of a clinical SPECT/CT, the GE Healthcare Optima NM/CT 640 (Healthcare n.d.).

5.4 Results

To create the system probability matrix, separate FWHM models were determined for the x dimension and the y dimension of the collimator because of the different responses seen from the parallel hole direction and fanbeam hole direction. Using the GATE simulations for a point source at varying distances from the collimator, resultant spatial resolution measurements were determined for each collimator geometry in both the diverging and parallel directions. Measurements were quantified in terms of the FWHM at each distance and were found to be linear within the region of interest for all collimator lengths (18 camera model shown in (Fig. 5.3). The flat response in the diverging direction is due to the increasing FOV making the object appear small as it moves away from the imaging plane.

The simulated ring geometries resulted in a range of reconstructed tomographic resolutions from 0.4 cm to 4.7 cm (center of the FOV) (Fig. 5.4). Even with fewer projection

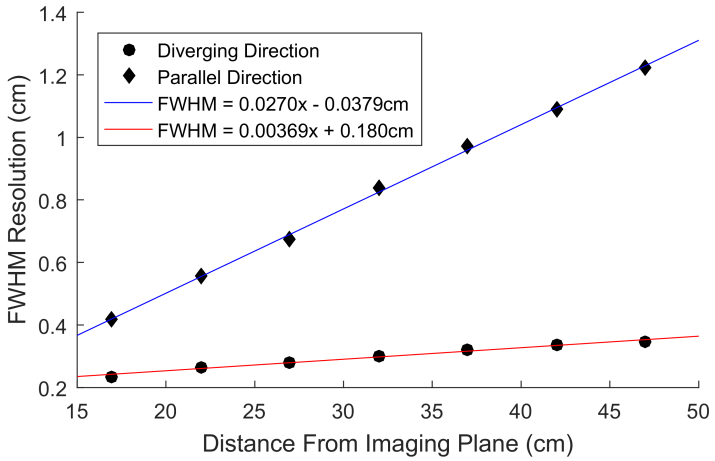

FIGURE 5.3: FWHM resolution models for the 18 camera, 3.83 cm collimator. Separate models are shown for the diverging direction and parallel direction. A linear regression fit was used with R2 values of 0.99 and 0.98 respectively. Statistical error bars smaller than symbol size.

angles, spatial resolution was found to still improve with longer collimators, however a limit of ∼8 mm was found regardless of collimator length. This resolution limit is likely limited to the intrinsic spatial resolution of the 2.46 mm detector pixel size and collimator hole size chosen, and from the scaling from 25 cm FOV to 7.9 cm camera size. To improve the resolution further, the system would require smaller sized pixels and/or corresponding matching collimators.

When compared to a conventional rotating, dual head camera with low energy high resolution parallel hole collimation (GE Optima 640), a comparable spatial resolution performance was achieved from the 18 camera, 3.83 cm collimator geometry. For this configuration, the sensitivity was found to be 7.0 times greater than that of the clinical GE system (Fig. 5.5). This improvement is principally due to the increased number of detector modules acquiring simultaneously in the stationary system.

Based on these results, we then performed a series of Monte Carlo simulations using multiple point sources in air in order to measure the reconstructed spatial resolution of tomographic data obtained from this geometry. We have used a custom ML-EM

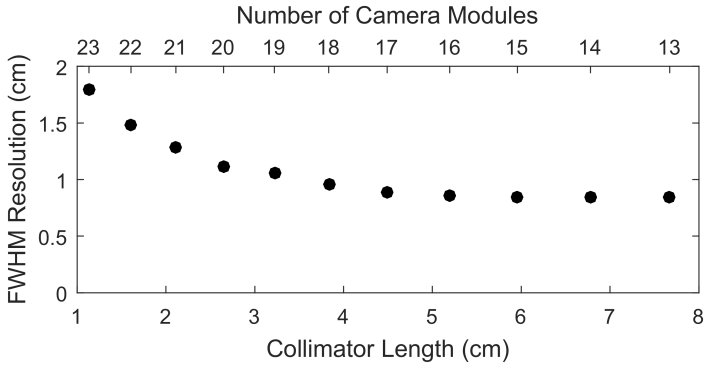

FIGURE 5.4: Comparison of tomographic resolution to the length of the diverging collimator. Three sigma error bars from FWHM Gaussian fit are smaller than symbol size.

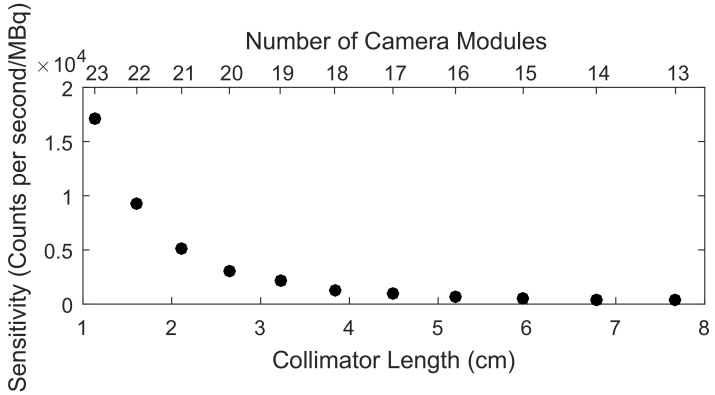

FIGURE 5.5: Comparison of system sensitivity to the length of the diverging collimator. Statistical error bars smaller than symbol size.

reconstruction algorithm with 100 iterations, without any subset acceleration. Projection data consisted of low-noise projections in order to reduce the influence of noise on reconstructed image resolution.

In the case of 18 camera views with 3.83 cm collimators, reconstructed spatial resolution across the x-y plane was found to vary by a factor of 2.2 (Fig. 5.6), with the worst resolution in the center and improvement towards the corners of the images. In the z-direction, resolution was found to remain relatively constant over the 7.9 cm axial length because of the parallel collimator geometry in the axial direction. A smearing

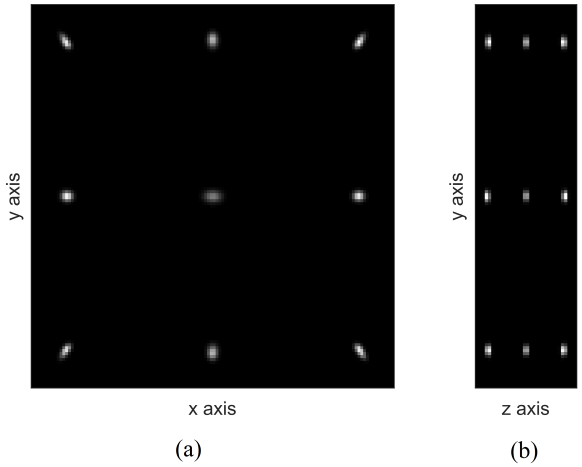

FIGURE 5.6: Sample slices of reconstructed point sources from a GATE simulation for an 18 camera, 3.83 cm collimator length, detector ring.

artifact was found to occur in the corners of the x-y FOV. This is believed to be due to undersampling within those regions. Effects such as this are expected to deteriorate the image quality further when using even less projection angles.

Further to the point source simulations, we used a more complicated hot-rod phantom to evaluate reconstructed image resolution. This was performed as an analytical simulation which simulated six rods situated in air. The rods had diameter sizes ranging from (12.7 to 4.8 mm) filled with identical concentrations of Tc-99m and . Again, projection data was reconstructed using the custom ML-EM reconstruction algorithm as used previously with 10000 iterations. The large number of iterations was found to improve the resolvability of the smaller details in the complex phantom.

Results of the reconstructed hot-rod phantom for the 18 camera setup (Fig. 5.7) matched the expected resolution performance with the three largest rod sizes (12.7 mm, 11.1 mm, and 9.5mm) being resolvable. As seen previously, the resolution did vary across the FOV with the 7.9 mm diameter rod size found to be the most resolvable on the outside of the FOV and worse towards the center. All rod sizes of 7.9 mm diameter or smaller suffered from aliasing effects and were unresolvable as seen previously. Again,

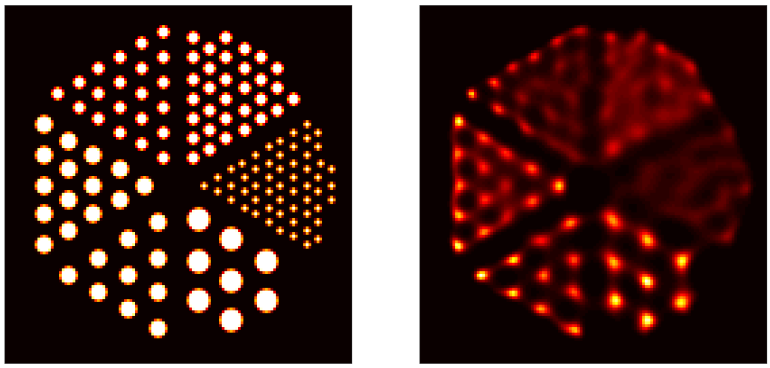

FIGURE 5.7: (a) hot-rod phantom used for analytical simulation. (b) Reconstructed phantom using 18 camera, 3.83 cm collimator FWHM model. The largest size rod (12.7 mm) and second largest size rod (11.1 mm) can be fully resolved. The third largest size rod (9.5 mm) is partially resolvable.

this is consistent with the 2.46 mm pixel size of the detectors and the corresponding pixel-matched collimator square hole size.

Further analytical hot-rod phantom simulations used to investigate alternative design options demonstrated how the resolvability is affected by collimator size, pixel size, and number of projection angles (Fig. 5.8). When compared to the standard 18 camera 1:1 pixel matched result, reduction of collimator hole size to a 4:1 pixel match improved resolution, allowing the next smallest rod size (7.9 mm) to be resolved. Although this design would have slightly reduced sensitivity, it does demonstrate the capability of further performance from the current CZT detectors while maintaining limited space constraints. The further reduction of pixel size (pixel density increased by a factor of four) resulted in further improvement of resolution, again allowing the next smallest rod size (6.4 mm) to be resolved. Finally, increasing the number of projection angles was found to remove the additional smearing artifacts found throughout the reconstructions. However, it did not significantly improve resolution, with the same resolvable limit in each case.

5.5 Conclusions

We have performed an investigation into possible full-ring SPECT camera designs for simultaneous SPECT/MR imaging. Results appear to indicate that a full-ring, diverging fan beam collimator system could be capable of offering similar resolution performance to current conventional rotating, parallel-hole clinical systems and even offer improved sensitivity. We have found that an 18 camera system with 3.83 cm length diverging collimators offered the closest performance to the clinical system but is limited in spatial resolution due to the intrinsic detector resolution. Nevertheless, this geometry is promising and could be a viable option for a multimodal SPECT/MR system moving forward.

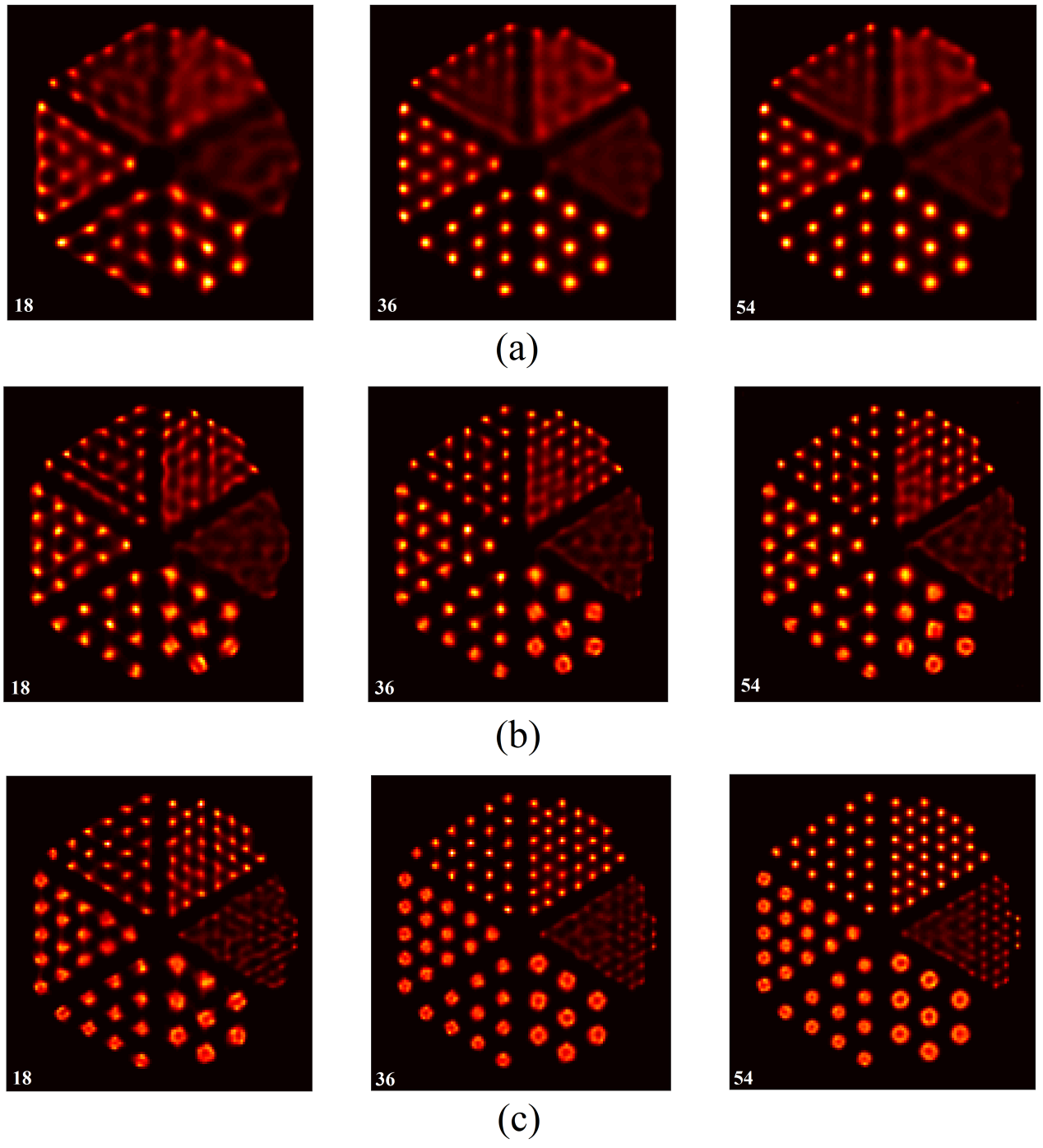

FIGURE 5.8: Analytical hot-rod phantom simulations for varying design parameters. All simulations used a 3.83cm collimator with 18, 36, and 54 projection angles. (a) 2.46 mm pixels with 1:1 pixel matched collimator. (b) 2.46 mm pixels with 4:1 pixel matched collimator. (c) 1.23mm pixels with 1:1 pixel matched collimator.

Chapter 6

Discussion and Conclusions

6.1 Discussion

Although the MR images were found to suffer considerably from SNR degradation during simultaneous operation, successfully proof of concept was achieved. The hardware and software that was developed was capable of acquiring a gamma camera image during an MRI scan of which approached clinical sequence parameters. Several key design choices are worth noting and will be discussed here.

First, the operating frequencies of the electronics within the MRI bore were found to have a considerable effect on the MR image quality. Use a microcontroller with a 600 MHz processor clock and use of Bluetooth communication operating at 2 GHz were both found to improve MRI SNR. However, the communication between the microcontroller and the CZT detector modules were still set at 15 MHz with a maximum hardware limit of 24 MHz. Although this frequency does not approach the MRI's standard operating frequency of 128 MHz, it is postulated that higher harmonics of the fundamental frequency may still be causing interference. Although the camera is currently limited by the CZT detector's ASIC maximum communication speed, future designs may look at other CZT detector options which could allow for higher communication speeds at

greater than 128 MHz to further improve the MRI SNR. Alternatively, the high frequency components of the clock's digital square wave could potentially be reduced by using a low pass filter which would convert the square wave into a sine wave. However further testing would need to be done to determine if this is a viable solution that the system could still reliably work under.

Secondly, the PCB design was found to be sufficient for testing of the mutual interference effects, however SPI communication was limited to ∼15MHz. Beyond this communication speed, the traces were subject to reflection noise. Greater care for high speed communication PCB design should remove this issue. Although this communication speed was not found to limit the count rate for any of the tests performed thus far, it could potentially limit future experiments using hotter sources. Additionally, the option of two additional ground plane layers on either side of the PCB may help to shield the emitted EMI without significant changes to the design.

Thirdly, although the design is modular with the concept of using multiple camera modules to form a full SPECT ring, this process is not expected to be trivial. In particular, the Bluetooth communication of many separate microcontrollers back to the main master PC computer could lead to software complexities and imprecise synchronization of the many cameras. It may be necessary to develop new hardware and software where a master microcontroller is capable of communicating with each camera module microcontroller and all communication is done through a single Bluetooth connection. This design would have a master module which would directly communicate to the master PC and would control each of the individual camera modules which form the ring.

The thesis also looks at the potential of a fanbeam collimator geometry for the SPECT/MR system. Although this geometry is suggested as a potential design moving forward, a more rigorous testing of the collimator and additional parameter options should be evaluated. First, the analytical simulations for the hot-rod phantoms were not

subject to additional noise such as scatter, and background detector noise. Factors such as these will reduce image quality and may impact the potential geometry chosen. Secondly, the reconstruction algorithm did not take into account attenuation factors. More rigorous testing of more complex phantoms would then be possible. This could allow for a more realistic comparison of collimator performance, particularly when comparing the qualitative effects of the smearing artifacts seen from undersampling.

6.2 Conclusions

This thesis investigated the option of using a CZT detector gamma camera system for simultaneous SPECT/MR imaging. The camera was designed and built with the design requirements to be safe in an MRI environment and to fit into a SPECT ring which could be inserted into an existing MRI. Initial testing of the design did show considerable SNR degradation to the MR image during simultaneous acquisition, and showed that MR RF pulses and gradients were found to cause unreliable performance from the CZT detectors. It was found that large increases in the CZT detector count rate directly correlated with the application of the magnetic field gradient switching. The use of a gradient trigger circuit to gate the gamma camera acquisition during gradient switching phases was investigated in order to remove this mutual interference effect. Testing of this new triggering protocol now shows reliable performance from the gamma camera during simultaneous imaging. Successful coregistration of the two images was achieved with the produced images showing no structural differences when compared to control acquisitions taken without an MRI sequence running. However due to the additional deadtime from triggering, the total counts were 60% lower than the control and the MR image was still found to have 92% reduction in SNR.

This thesis also presents the option of a diverging collimator design for the SPECT ring insert. The results of the simulations appear to indicate that a full-ring, diverging

fan beam collimator system could be capable of offering similar resolution performance to current conventional rotating, parallel-hole clinical systems and even offer improved sensitivity. In particular, an 18 camera system with a 3.83 cm length diverging collimator offered the closest performance.

Chapter 7

Future Work

During the simultaneous imaging testing, no geometric distortions were found in either the MR or gamma camera projection images. However the MRI SNR was found to the degraded significantly compared to the control image. The first course of future work should look at potential ways to to reduce this noise through: (1) changing the communication frequency, (2) additional PCB EMI reduction techniques, and (3) exterior shielding of the gamma camera system using a Faraday cage method.

For the gamma camera performance, a better understanding of how the MRI is affecting the individual components of the camera should be achieved. It is still unknown why the microcontroller is unable to operate during MRI sequences with a flip angle greater than 30 degrees or whether there is a way to solve this problem. For a fully clinical system, the SPECT system should be able to operate with any MRI sequence. This incompatibility between the two systems should be investigated using the MR device testing facility at Western University. At this facility, individual components of the camera module can be exposed to specific RF flipping pulses of known power and variable shape in isolation of the other effects found in a full MRI machine. This process could potentially help to determine the exact cause and a potential solution to the limit on flip angle sequences.

For the collimator design, additional parameters such as the material of choice should be investigated. More complex phantoms such as a Zubal Brain Phantom should also be simulated to provide a stronger comparison of geometry performance. Next, a manufacturing method such as rapid additive manufacturing must be developed for such a custom design. Finally the simulation results should be compared to a manufactured model for validation.

Appendix A

Appendix

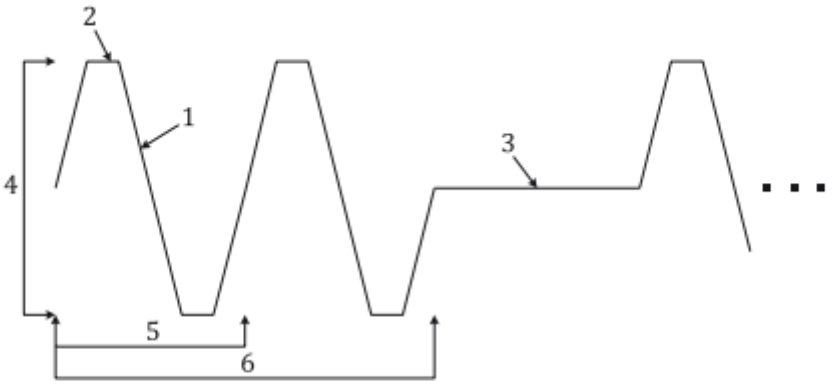

Key

1 t_{slew} (min to max rise/fall time in ms)
2 t_{dwell}
3 t_{off} (time between bursts)
4 B_g (magnetic field strength produced by gradient, min to max amplitude in mT)
5 one cycle
6 burst length (two cycles in this example)

FIGURE A.1: Gradient waveform timing parameter diagram. Sequence parameters are taken from the technical standard ISO/TS 10974.

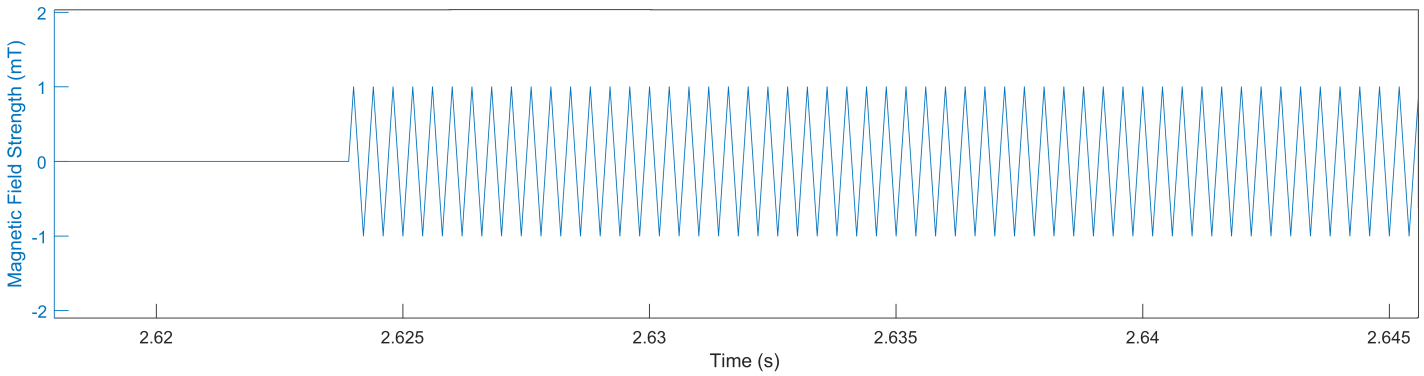

Figure A.2: Simulated gradient shape of the first test sequence.

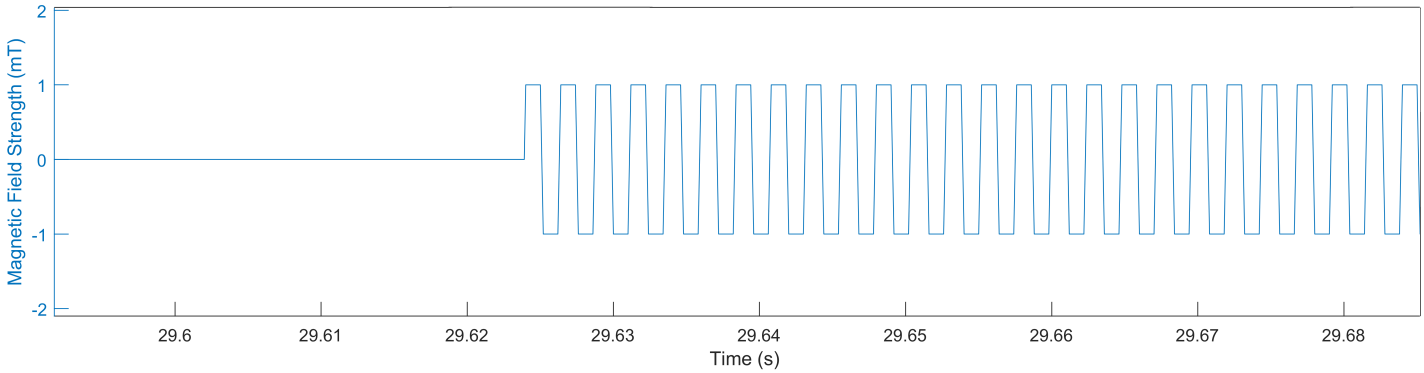

Figure A.3: Simulated gradient shape of the second test sequence.

Table A.1: Table of the 31 Gradient Sequence Parameters.

$t_{slew}(ms)$	$t_{dwell}(ms)$	$t_{off}(ms)$	$B_g(mT)$	$t_{one_cycle}(ms)$	burst length
0.2	0	0	0.2	0.4	128
0.2	1	0	0.2	2.4	128
0.2	5	0	0.2	10.4	128
0.2	20	0	0.2	40.4	128
0.2	0	5	0.2	0.4	128
0.2	1	5	0.2	2.4	128
0.2	5	5	0.2	10.4	128
0.2	20	5	0.2	40.4	128
0.2	0	100	0.2	0.4	128
0.2	1	100	0.2	2.4	128
0.2	5	100	0.2	10.4	128
0.2	20	100	0.2	40.4	128
0.2	0	500	0.2	0.4	128
0.2	1	500	0.2	2.4	128
0.2	5	500	0.2	10.4	128
0.2	20	500	0.2	40.4	128
1.0	0	0	0.296	2	128
1.0	1	0	0.296	4	128
1.0	5	0	0.296	12	128
1.0	20	0	0.296	42	128
1.0	0	5	0.296	2	128
1.0	1	5	0.296	4	128
1.0	5	5	0.296	12	128
1.0	20	5	0.296	42	128
1.0	0	100	0.296	2	128
1.0	1	100	0.296	4	128
1.0	5	100	0.296	12	128
1.0	20	100	0.296	42	128
1.0	0	500	0.296	2	128
1.0	1	500	0.296	4	128
1.0	5	500	0.296	12	128

Bibliography

Accorsi, R. (2008). Brain Single-Photon Emission CT Physics Principles. *American Journal of Neuroradiology* 29(7), 1247–1256.

Advatech UK - Overview of CZT Radiation Detectors (n.d.). https://www.advatech-uk.co.uk/overview_czt_detectors.html. Accessed: 2021-01-5.

Audenhaege, K. (2015). Review of SPECT collimator selection, optimization, and fabrication for clinical and preclinical imaging. *Med. Phys.* 42(8), 4796–4813.

Bailey, D. (2013). An Evidence-Based Review of Quantitative SPECT Imaging and Potential Clinical Applications. *Journal of Nuclear Medicine* 51(1), 83–89.

Branderhorst, W. (2010). Pixel-based subsets for rapid multi-pinhole SPECT reconstruction. *Physics in Medicine Biology* 55(7).

Cai, L. (2013a). Hybrid pixel-waveform CdTe/CZT detector for use in an ultrahigh resolution MRI compatible SPECT system. *Nuclear Instruments and Methods in Physics Research* 702.

Cai, L. (2013b). MRC-SPECT: A sub-500 mm resolution MR-compatible SPECT system for simultaneous dual-modality study of small animals. *Nuclear Instruments and Methods in Physics Research* 734, 147–151.

Canadian Healthcare (2018). https://www.canhealth.com/2018/07/03/toronto-hospitals-advance-scope-of-imaging-with-pet-mr/. Accessed: 2021-01-5.

Carminati, M. (2018). SPECT/MRI INSERT Compatibility: Assessment, Solutions, and Design Guidelines. *IEEE Transactions on Radiation and Plasma Medical Sciences* 2(4), 2469–7311.

Carminati, M. (2019). Validation and Performance Assessment of aPreclinical SiPM-Based SPECT/MRI Insert. *IEEE TRANSACTIONS ON RADIATION AND PLASMA MEDICAL SCIENCES,* 3(4), 484–490.

Cherry, S. (2004). In vivo molecular and genomic imaging: new challenges for imaging physics. *Phys. Med. Biol.* (49), 13–48.

Crestani, R. (2010). Redlen Digital Module Specification. *Redlen Technologies Inc.*

Ehman, E. (2017). PET/MRI: Where Might It Replace PET/CT? *Journal of Magnetic Resonance Imaging* 46(5), 1247–1262.

GE SIGNA™ PET/MR (n.d.). https://www.gehealthcare.com/products/magnetic-resonance-imaging/3-0t/signa-pet-mr. Accessed: 2021-01-5.

Geotz, C. (2008). SPECT Low-Field MRI System for Small-Animal Imaging. *The Journal of Nuclear Medicine* 49(1), 88.

Hamamatsu (n.d.). *S10931-3050P*. Vol. 1. Hamamatsu.

Hamamura, M. (2010). Development of an MR-compatible SPECT system (MRSPECT) for simultaneous data acquisition. *Physics in Medicine and Biology* 55, 1563–1575.

Healthcare, G. E. (n.d.). *Parallel Hole Data Sheet*.

Hutton, B. (2016). Development of clinical simultaneous SPECT/MRI. *Br J Radiol* 91(1), 1081.

Hutton, B. (2018). Advances in clinical molecular imaging instrumentation. *Clinical and Translational Imaging* 6(1), 31–45.

Ideas SRE4001 (n.d.). https://ideas.no/products/sre4001-and-sre4002/. Accessed: 2021-01-5.

Iniewski, K. (2014). CZT detector technology for medical imaging. *Journal of Instrumentation* 9(11), C11001.

Lai, X. (2018). Simulation study of the second-generation MR-compatible SPECT system based on the inverted compound-eye gamma camera design. *Physics in Medicine and Biology* 63(1), 12.

Lee, S. (2014). Targeted multimodal imaging modalities. *Adv. Drug Deliv. Rev.* (76), 60–76.

Meier, D. (2011). A SPECT camera for combined MRI and SPECT for small animals. *Nuclear Instruments and Methods in Physics Research* 652(1), 731–734.

Mueller, B. (2003). Evaluation of a small cadmium zinc telluride detector for scintimammography. *J. Nucl. Med.* 44(4), 602–609.

Muzic Jr., R. (2014). PET/MRI - Technical Review. *Seminars in Roentgenology* 49(3), 242–254.

National Research Council (US) (1996). *Mathematics and Physics of Emerging Biomedical Imaging*. Vol. 1. National Academies Press (US).

Patton, J. (2009). Hybrid Imaging Technology: From Dreams and Vision to Clinical Devices. *Semin. Nucl. Med.* (39), 247–263.

Polyakov, S. (n.d.). *Experimental Methods in the Physical Sciences*.

Salvado, D. (2014). Novel Collimation for Simultaneous SPECT/MRI. *IEEE Nuclear Science Symposium and Medical Imaging Conference*.

SensL - Introduction to SiPM (2011). https://www.sensl.com/downloads/ds/TN%20-%20Intro%20to%20SPM%20Tech.pdf. Accessed: 2021-01-5.

Shepp, L. (1982). Maximum Likelihood Reconstruction for Emission Tomography. *IEEE TRANSACTIONS ON MEDICAL IMAGING* 1(2), 113–122.

Stanford (2009). https://web.stanford.edu/group/scintillators/imgfund/pmt.jpg. Accessed: 2021-01-5.

Tao, A. (2016a). Measuring the Mutual Effects of a CZT Detector and a 3T MRI for the Development of a Simultaneous MBI/MRI Insert. *IEEE Trans. Nucl. Sci.* 63(5), 2558–2566.

Tao, A. (2012). Development of a Silicon Photomultiplier Based Gamma Camera. *McMaster MacSphere*.

Tao, A. (2016b). Advanced Methods in Molecular Breast Imaging. *Ph.D. Dissertation, Med. Phys., McMaster University, Hamilton, Ontario.*

Trigilio, P. (2018). A SiPM-Readout ASIC for SPECT Applications. *IEEE TRANSACTIONS ON RADIATION AND PLASMA MEDICAL SCIENCES* 2(5), 404–410.

Wagenaar, D. (2006). Development of MRI-Compatible Nuclear Medicine Imaging Detectors. *IEEE Nuclear Science Symposium Conference Record*, 1825–1828.

Wagenaar, D. (2007). Advantages of semiconductor CZT for medical imaging. *Proceedings of SPIE* 6707(1).

Wehner, J. (2014). PET/MRI insert using digital SiPMs: Investigation of MR-compatibility. *Nuclear Instruments and Methods in Physics Research* 734(2), 116–121.

Weishaupt, D. (2006). *How does MRI work?: An Introduction to the Physics and Function of Magnetic Resonance Imaging*. Vol. 2. Springer.

WHO - public health challenges (2006). https://www.who.int/mental_health/neurology/neurological_disorders_report_web.pdf?ua=. Accessed: 2021-01-5.

WHO - World Health Report (2001). https://www.who.int/whr/2001/media_centre/press_release/en/. Accessed: 2021-01-5.

Yang, C. (2018). PET-MR and SPECT-MR multimodality probes: Development and Challenges. *Theranostics* 8(22), 6210–6132.

Zhang, Y. (2020). Advances in multimodal data fusion in neuroimaging: Overview, challenges, and novel orientation. *Information Fusion* 64(1), 149–187.